Nanoscale

PAPER

View Article Online
View Journal | View Issue

Cite this: *Nanoscale*, 2026, **18**, 7564

Translating magnetic fluid hyperthermia toward lung cancer treatment

Malgorzata Sikorska, *[a] Magdalena Bamburowicz-Klimkowska, [a] Monika Ruzycka-Ayoush, [a] Anna M. Nowicka, [b] Agata Kowalczyk, [b] Artur Kasprzak, [c] Grzegorz Domanski, [d] Barbara Wagner, [e] Monika Prochorec-Sobieszek, [f] Marzena Cabaj, [f] Anna Szumera-Ciechkiewicz, [g] Maciej Glogowski, [h] Andrzej Cieszanowski [i] and Ireneusz P. Grudzinski *[a]

Magnetic fluid hyperthermia (MFH) emerges as a potential new therapeutic strategy for the treatment of lung cancer. However, the biological endpoints underpinning its therapeutic efficacy remain insufficiently defined in this tumor. In this work, we advance the translational potential of MFH by delineating metabolic, structural and biophysical endpoints in patient-derived lung cancer models. Specifically, we evaluated the effects of MFH using $Mg_{0.1}$-γ-Fe_2O_3(mPEG-silane)$_{0.5}$ nanoparticles (NPs) subjected to an alternating magnetic field (AMF) on patient-derived lung cancer cells (*in vitro*) and NUDE Balb/c mice bearing patient-derived lung cancer xenografts, PDX (*in vivo*). We elucidated that MFH induces metabolic dysfunction in lung cancer cells, leading to reduced proliferation, diminished colony formation and restricted cell migration. Moreover, alterations in metallomic profiles and changes in glycan structures were detected in lung cancer cells treated with MFH. These were accompanied by released matrix metalloproteinases (MMP-1, MMP-2, and MMP-9) and increased cell membrane permeability, indicating that the primary effect of MFH on human lung cancer cells targets membrane integrity and the cell–extracellular matrix environment. Studies have shown that mice bearing lung cancer PDX subjected to MFH experienced a significant reduction in tumor growth compared to the untreated control. The CEM43 value, representing the cumulative equivalent minutes at 43 °C, was estimated to be approximately 9.1 minutes in MFH-treated animals, while the specific absorption rate (SAR) ranged between 389 and 475 W g^{-1}. Together, these findings refine the characterization of hyperthermia treatment endpoints and demonstrate magnetic fluid hyperthermia as a promising translational approach for lung cancer therapy, meriting further evaluation in future clinical applications.

Received 29th November 2025,
Accepted 28th January 2026

DOI: 10.1039/d5nr05036g

rsc.li/nanoscale

1. Introduction

The concept of using heat to destroy cancer dates back to ancient times.[1] This therapeutic approach, termed hyperthermia, takes advantage of the fact that malignant cells exhibit lower tolerance to elevated temperatures compared to normal cells owing to their elevated metabolic activity and hypoxic environment of tumor tissues.[2,3] For decades, investigations have focused on elucidating the cellular and molecular consequences of thermal stress, including alterations in metabolic pathways and the induction of various forms of cell death.[4] The physiological and molecular effects of hyperthermia are highly temperature-dependent, offering opportunities to achieve specific therapeutic outcomes.[5] Elevated thermal stress may induce a range of intracellular alterations and, among others, result in the disruption of cellular homeostatic mechanisms.[6] Moreover, protein denaturation and aggregation induced by hyperthermia lead to the increased expression of

[a]*Department of Toxicology and Food Science, Faculty of Pharmacy, Medical University of Warsaw, 1 Banacha St., PL-02-097 Warsaw, Poland. E-mail: malgorzata.sikorska@wum.edu.pl, ireneusz.grudzinski@wum.edu.pl*
[b]*University of Warsaw, Faculty of Chemistry, 1 Pasteura St., PL-02-093 Warsaw, Poland*
[c]*Department of Organic Chemistry, Faculty of Chemistry, Warsaw University of Technology, 3 Noakowskiego St., PL-00-664 Warsaw, Poland*
[d]*Institute of Radioelectronics and Multimedia Technology, Faculty of Electronics and Information Technology, Warsaw University of Technology, 15/19 Nowowiejska St., PL-00-665 Warsaw, Poland*
[e]*University of Warsaw, Faculty of Chemistry, Biological and Chemical Research Centre, 101 Zwirki i Wigury St., PL-02-089 Warsaw, Poland*
[f]*Department of Hematology Diagnostics, Institute of Hematology and Transfusiology, 14 Indiry Gandhi St., PL-02-776 Warsaw, Poland*
[g]*Department of Cancer Pathomorphology, Maria Sklodowska-Curie National Research Institute of Oncology, 5 Roentgena St., PL-02-781 Warsaw, Poland*
[h]*Department of Lung Cancer and Chest Tumors, Maria Sklodowska-Curie National Research Institute of Oncology, 5 Roentgena St., PL-02-781 Warsaw, Poland*
[i]*Department of Clinical Radiology, Medical University of Warsaw, 1 Banacha St., PL-02-097 Warsaw, Poland*

heat shock proteins, a class of molecular chaperones possessing cytoprotective and anti-apoptotic functions, mediated through the stress-responsive transcription factor heat shock factor 1 (HSF1). These proteins facilitate the refolding of aberrant polypeptides and contribute to the removal of proteins that have sustained irreversible damage under diverse stress conditions.[7] Heat shock can also induce cytoskeletal reorganization (*e.g.*, actin, tubulin, and intermediate filaments)[8,9] and activate protective autophagy, a process mediated by endoplasmic reticulum stress.[10] Increased temperatures enhance the fluidity and, consequently, the permeability of cellular membranes, which can result in ion leakages.[11,12] A notable outcome of this process is the dissipation of the proton gradient across the mitochondrial inner membrane (*i.e.*, mitochondrial uncoupling), causing a transient reduction in mitochondrial ATP synthesis.[13] Hyperthermia causes DNA damage in cancer cells, for instance by diminishing telomerase activity,[14] and prompts changes in their gene expression patterns.[15] Further effects have been extensively discussed by other researchers, with Yi *et al.*[16] offering a wide review on this subject.

Of particular relevance within the field of selective thermal therapies is magnetic fluid hyperthermia (MFH), a modality that utilizes magnetic nanoparticles (NPs) as localized mediators of heat generation.[17] When exposed to an alternating magnetic field (AMF), these NPs dissipate energy primarily through hysteresis losses and relaxation processes. The oscillation of magnetic moments induces domain wall displacement, resulting in heat production. Following removal of the external field, magnetic moments return to equilibrium *via* two principal pathways: the reorientation of magnetic moments within the particles, termed Néel relaxation, and the physical rotation of NPs around their axes, known as Brownian relaxation.[18] Consequently, the application of MFH not only enables the induction of heat-mediated cell death mechanisms discussed previously but also permits selective cytotoxicity, sparing surrounding healthy tissues. Magnetic NPs constitute a major focus of ongoing research, as their composition, size, and surface chemistry can be precisely engineered to elicit specific biological responses. Functionalization with additional moieties, such as targeting ligands, chemotherapeutic agents, or imaging contrast agents, has the potential to enhance therapeutic and diagnostic efficacy and expand multifunctionality, also called theranostics.[19] Nevertheless, despite substantial progress, challenges persist in achieving sufficiently high specific absorption rates (SARs) while maintaining safety, biocompatibility, and precise control over heating efficiency. MFH remains a promising anticancer modality under continuous development in multiple research directions.[20,21] We recently reported a novel class of magnesium-doped magnetic NPs, specifically engineered to combine enhanced biocompatibility with superior magnetic properties – an effect not observed with other metal dopants (please see Nowicka *et al.*).[22,23] This design provides a novel approach for enhancing nanoparticle-mediated magnetic hyperthermia for targeted cancer therapy.

Among the currently available thermal cancer therapies, MFH has gained increasing attention due to its distinct therapeutic and technological advantages. This modality enables highly localized heating of tumor tissue through the application of an AMF to magnetic NPs selectively accumulated within the tumor, thereby effectively minimizing thermal damage to surrounding healthy tissues. MFH offers precise spatial and temporal control over temperature distribution, resulting in improved treatment selectivity and reproducibility.[24] Moreover, owing to the efficient penetration of the AMF through biological tissues without significant attenuation, MFH represents a minimally invasive strategy suitable for the treatment of deeply seated tumors. Importantly, numerous preclinical and clinical studies have demonstrated that MFH can enhance the efficacy of conventional cancer therapies, such as chemotherapy and radiotherapy, through synergistic mechanisms including increased tumor perfusion, enhanced drug delivery, and improved radiosensitivity.[25,26] These combined therapeutic approaches may lead to superior tumor control while concurrently reducing systemic toxicity and adverse side effects.[24] A concise comparison of cancer thermal therapies based on the currently available literature is presented in Table 1.[27–30]

A mechanistic understanding of MFH-induced cellular responses, especially membrane-mediated pathways, remains limited. Here, we demonstrate a membrane-targeted mechanism, offering unprecedented insight into how MFH disrupts lung cancer cellular integrity. To demonstrate translational relevance, we employed patient-derived lung cancer cells, addressing therapy in a clinically meaningful context and evaluated MFH efficacy in patient-derived xenografts using NUDE Balb/c mice as models.[36] These models preserve primary tumor features, including genetic heterogeneity, microenvironmental interactions, and intrinsic resistance mechanisms, bridging *in vitro* findings with *in vivo* outcomes. Collectively, this work presents a novel integrative framework for advancing targeted, hyperthermia-based lung cancer therapies and establishes a foundation for future clinical translation.

2. Experimental

2.1 Synthesis of magnesium-doped iron(III) oxide nanoparticles

The synthesis of magnesium-doped iron(III) oxide nanoparticles ($Mg_{0.1}$-γ-Fe_2O_3(mPEG-silane)$_{0.5}$) was conducted *via* the thermal decomposition method. A comprehensive account of this synthesis, along with the corresponding physicochemical and magnetic characterization, has been detailed in the recent publication.[22] Recent studies have also been published, demonstrating the lack of cytotoxicity and genotoxicity of the as-synthesized $Mg_{0.1}$-γ-Fe_2O_3(mPEG-silane)$_{0.5}$ NPs, despite their cellular uptake in both cancerous and noncancerous lung cells.[23]

Table 1 Comparison of magnetic fluid hyperthermia with other thermal therapies.[27–30] The "Ref." (References) column lists representative publications for each therapeutic modality

Method of thermal therapy	Mechanism	Advantages	Disadvantages	Ref.
Magnetic Fluid Hyperthermia (MFH)	Magnetic nanoparticles generate heat under an alternating magnetic field (Néel and Brownian losses).	Very high spatial selectivity. Effective for deep-seated tumors. Minimally invasive, cost-effective technique associated with reduced infection risk and quicker recovery.	Non-uniform particle distribution. Safety limits on the field amplitude and frequency. Limited large-scale clinical adoption.	31
Radiofrequency Ablation (RFA)	Heat is produced when alternating electrical current moves through ion-rich tissue, causing charged particles to vibrate rapidly and generate thermal energy that then spreads to surrounding areas by heat diffusion. The electrical current is delivered directly to the targeted area.	Minimally invasive, cost-effective technique associated with reduced infection risk and quicker recovery. Most commonly used modality and the standard treatment *e.g.* for primary and secondary liver cancers.	Requires the use of grounding pads, which may lead to skin burns, and depends on tissue with adequate electrical and thermal conductivity. Limited by its strong dependence on tissue electrical properties, as low water content (*e.g.* in the lungs) and heat-induced dehydration increase impedance, reduce power delivery, and slow effective heat generation.	32
Microwave Ablation (MWA)	Electromagnetic waves cause polar water molecules in tissue to rapidly rotate as the electric field alternates, especially when the frequency matches their natural resonance. Rapid molecular motion generates heat through friction, which at sufficient levels leads to cell death by coagulative necrosis.	Generates higher temperatures, produces larger ablation zones more rapidly, and provides more efficient heat distribution than RFA. It does not require grounding pads. More effective in tissues with strong heat-sink effects or low electrical and thermal conductivity, such as the liver, kidneys, lungs, and bone.	Limited by thick cables that can overheat and damage the surrounding tissue, and by large probes that produce long, unpredictable ablation zones.	33
Laser Interstitial Thermal Therapy (LITT)	Heat is generated as photon energy is converted into molecular motion, and this rise in motion energy ultimately leads to tissue damage.	The small diameter of laser fibers allows precise application, making the technique particularly suitable for small organs such as the prostate. MRI compatibility allows precise temperature and thermal dose monitoring, enabling accurate treatment of tumors in difficult locations (*e.g.*, brain and prostate) while sparing adjacent critical neural tissues.	High temperatures close to the laser fiber can induce tissue carbonization, limiting light transmission and ablation growth, while the small treatment volume often necessitates repeated fiber repositioning or multiple fibers for larger targets.	34
High Intensity Focused Ultrasound (HIFU)	Mechanical energy converted to heat and acoustic cavitation, delivered *via* internal or external ultrasound devices.	Primarily applied to easily accessible, relatively motionless sites, such as uterine and breast fibroids and benign prostatic hyperplasia. Enables non-invasive tissue ablation using non-ionizing energy.	Best for stationary organs like kidneys and prostate due to long treatment times, shallow penetration and requirement for a clear acoustic window.	35

2.2 Patient derived lung cancer cells (H22/987)

All experiments were performed in accordance with the Guidelines of the Declaration of Helsinki and were approved by the Bioethics Committee of the Maria Sklodowska-Curie National Research Institute of Oncology (approval no. 35/2020). Written informed consent was obtained from all human participants of this study. Human primary lung cancer cells were derived from a patient coded H22/987 who underwent surgical removal of lung cancer.[36] The lung cancer specimen was processed immediately after resection. We fragmented the lung cancer tissues using sterile surgical blades into approximately 1 × 1 mm pieces. We then minced the fragments on a grid and seeded them on a plate in F-12K medium (Kaighn's modification of Ham's F-12 medium); Gibco, Paisley, supplemented with 10% fetal bovine serum (FBS; Gibco, Paisley, UK) and antibiotics (streptomycin, 50 μg mL^{-1}; amphotericin B, 1.25 μg mL^{-1}; gentamicin, 50 μg mL^{-1}; penicillin, 50 μg m L^{-1}) (Gibco, Paisley, UK). The culture medium was refreshed every two to three days in the first week of culturing, and cells underwent washing with phosphate-buffered saline to eliminate tissue debris. After establishing the primary cell culture, called here as H22/987 cells, we transferred the cells to T75 culture flasks (Gibco). The H22/987 cells were sub-cultured twice per week at 80–85% confluency. To facilitate detachment, the cells were incubated with trypsin-EDTA (0.25% trypsin/

EDTA solution; Gibco, Paisley, UK) for 3–5 minutes. Medium was added and the suspension was centrifuged to remove trypsin/EDTA before the cells were seeded in Corning CellBind® cell culture flasks.

2.3 Methods for the evaluation of *in vitro* magnetic hyperthermia treatment

To evaluate the effects of MFH, confirm its therapeutic efficacy and understand the underlying cellular mechanisms, we performed a series of cytotoxicity assays.

2.3.1 Alamar Blue (AB) assay. Cells (H22/987) were trypsinized and seeded in 35 mm Petri dishes at a density of 5×10^4 cells per dish in 2 mL of F-12 medium. After 24 hours of incubation, the cells were exposed to $Mg_{0.1}$-γ-Fe_2O_3(mPEG-silane)$_{0.5}$ NPs (250 μg mL^{-1}) and subsequently magnetized (18 mT and 21 mT) for 45 minutes with AMFs. Non-magnetized cells, both with and without NPs (250 μg mL^{-1}), served as controls. Both magnetized and non-magnetized cells were incubated for 24 hours. Following incubation, the control medium and the tested NPs were removed. The cells were rinsed twice with PBS, and 1 mL of AB solution (a 10% [v/v] solution of AB dye in fresh medium) was added to each dish. After 3 hours of incubation, the contents of each dish were transferred to a 96-well flat-bottom plate. Alamar Blue fluorescence was measured using an Epoch microplate reader (BioTek) at excitation and emission wavelengths of 560 and 590 nm, respectively, in accordance with established protocols.[37]

2.3.2 Trypan Blue (TB) assay. The study was conducted in a manner similar to the AB assay described in section 2.3.1. After 24 hours post-exposure to an AMF (18 mT), the culture medium was collected, and the cells (H22/987) were detached using trypsin. The harvested cells were centrifuged at 25 °C for 7 minutes at 130 rcf, and the resulting cell pellet was resuspended in 200 μL of medium. A mixture of 0.4% Trypan Blue (TB) solution and the cell suspension was prepared and assessed under a microscope for cell counting.[38]

2.3.3 Wound healing (WH) assay. The scratch assay was conducted following the procedure outlined by Liang *et al.*[39] In brief, H22/987 cells (50×10^5 cells per dish) were seeded in 35 mm Petri dishes containing cut inserts, allowing them to grow as a monolayer for 24 hours. Subsequently, the cells were exposed to $Mg_{0.1}$-γ-Fe_2O_3(mPEG-silane)$_{0.5}$ NPs (250 μg mL^{-1}), and then subjected to magnetization for 45 minutes using an AMF (18 mT). Control groups included non-magnetized cells treated both with and without NPs (250 μg mL^{-1}). After a 24-hour post-exposure period, a "scratch" was created by removing the insert from the dish. The detached cells were washed away with PBS and 2 mL of fresh F-12 medium was added, followed by a 48-hour incubation. Three replicates per concentration were prepared. The scratches were observed under a phase-contrast microscope and photographed at a reference point. The closure of the scratch was monitored at 0, 24 and 48 hours of the experiment using a microscope (Delta Optical NIB-100) at a magnification of ×4. The scratch images were analyzed using ImageJ and the scratch area was calculated. The cell migration towards the scratch was quantified as a percentage of scratch closure.

2.3.4 Colony forming efficiency (CFE) assay. On the initial day, the H22/987 cells were seeded at a density of 200 cells per dish in 2 mL of fresh complete medium in 35 mm Petri dishes. Following a 24-hour incubation period, the cells were exposed to $Mg_{0.1}$-γ-Fe_2O_3 (mPEG-silane)$_{0.5}$ NPs (250 μg mL^{-1} and 500 μg mL^{-1}) and then magnetized (18 mT) for 45 min with AMFs. Three replicates were performed for each concentration. Parallel studies included a positive control (sodium chromate, Na_2CrO_4, 100 μM), a negative control (medium) and a solvent control (ultrapure water). The cells were treated for 72 hours, after which the incubated medium with added compounds was removed and replaced entirely with fresh culture medium. On the 12th day from seeding the cells were fixed with a fixing solution of 10% (v/v) formaldehyde in PBS and stained with a staining solution of 10% (v/v) Giemsa in ultrapure water. The Petri dishes were air-dried before the colonies were counted. Colony counting was conducted using a stereoscopic microscope (Opti-Tech Scientific).

2.3.5 Assessment of metalloproteinases (MMPs). On the initial day, the H22/987 cells were seeded in 35 mm Petri dishes at a density of 25×10^5 cells per dish in 2 mL of fresh F-12 complete medium in three replicates. After 24 h of incubation, the cells were exposed to $Mg_{0.1}$-γ-Fe_2O_3(mPEG-silane)$_{0.5}$ NPs (250 μg mL^{-1}) and further magnetized for 45 min with AMF (18 mT). After a 24-hour post-exposure period, the cells along with the medium were collected in various ways for a precise analysis of MMP concentration at each stage of the experiment, as schematically shown in Fig. 1A. The obtained results were calculated relative to the amount of protein (mg L^{-1}).

For quantitative studies of the active form of MMP-1, MMP-2, and MMP-9 we used a novel voltammetric method, developed in-house,[40] based on the ability of active MMPs to hydrolyze the peptide bond between specific amino acids. MMP-1 shows high activity against the amino acid pair glycine–isoleucine (Gly–Ile); for MMP-2, the enzymatic cut is between leucine (Leu) and glycine (Gly); and MMP-9 shows catalytic activity against the pair glycine–methionine (Gly–Met). Using square-wave voltammetry as a detection method, the sensor's receptor layer was formed by appropriate dipeptides labeled with a suitable redox probe: a carboxyl derivative of anthraquinone, ferrocene, and methylene blue. The current signals of the oxidation or reduction processes of the used redox probes differed in their position on the potential axis, as shown in Fig. 1B. The parameter verifying the presence of a given active form of MMP in the analyzed solution was the changes (decrease) in the intensity of the current signal of the corresponding receptor. These changes are a consequence of the removal of the redox-labeled amino acid from the receptor layer as a result of hydrolysis of the peptide bond by the active form of metalloproteinases. The voltammetric measurement was performed in the pure PBS buffer after the sample had been in contact with the sensor for two hours.

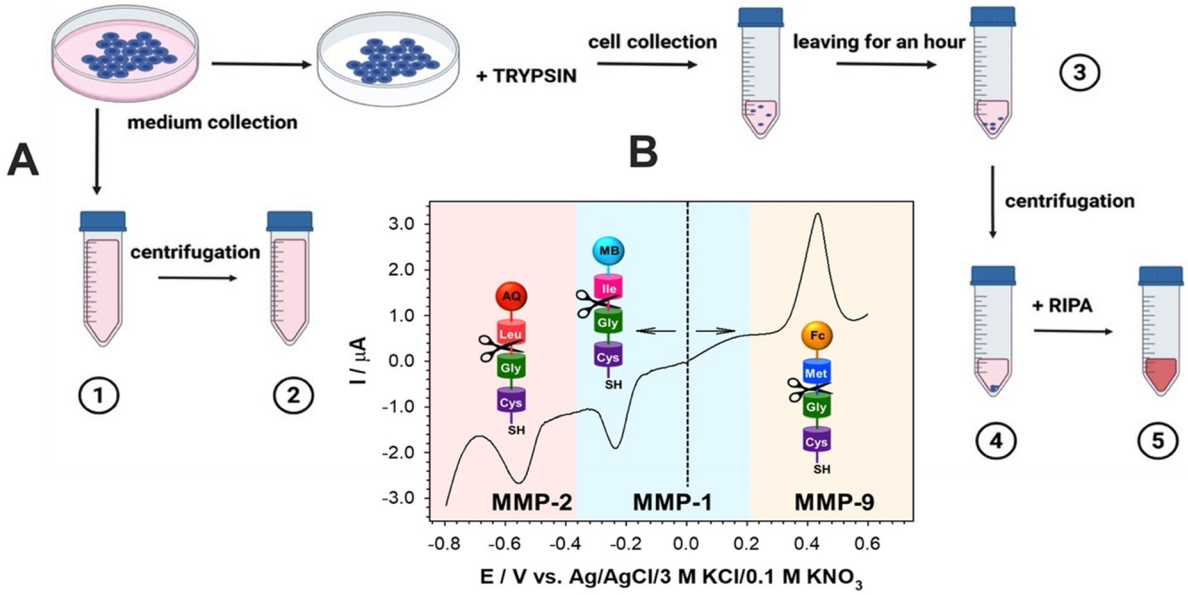

Fig. 1 (A) Scheme illustrating the procedure for collecting samples for the assessment of metalloproteinases (MMPs). The medium above the cells was collected (1) and centrifuged (2). The cells remaining on the dishes were detached with trypsin/EDTA, neutralized with medium and collected in Falcon tubes. These solutions were then allowed to settle. After an hour, samples were collected for the assessment of MMPs (3). The remaining Falcon tubes were centrifuged and after collecting a sample from the supernatant (4), RIPA solution was added (5). (B) Overview of a sensor-based method for analyzing MMP-1, MMP-2 and MMP-9.

2.3.6 Assessment of the glycan structure with a quartz crystal microbalance with dissipation (QCM-D). On the initial day, the H22/987 cells were seeded in 35 mm Petri dishes at a density of 25×10^5 cells per dish in 2 mL of fresh F-12 complete medium in three replicates. After 24 h of incubation, the cells were exposed to $Mg_{0.1}$-γ-Fe_2O_3 $(mPEG\text{-}silane)_{0.5}$ NPs (250 μg mL^{-1}) and further magnetized (18 mT) for 45 min with AMFs. Immediately after treatment, all cells were harvested and collected into Falcon tubes and then centrifuged at 25 °C for 7 minutes at 130 rcf. The resulting cell pellet was resuspended in 2000 μL of medium and reseeded onto new 35 mm Petri dishes containing QSense sensors. After 24 hours of incubation, an assessment was conducted. The experiments were performed with a QCM E4 instrument (Q-sense AB, Sweden) equipped with 4.95 MHz quartz crystals coated with polystyrene coated quartz crystals. Before the experiments the quartz crystals were immersed in 1% Deconex 11 water solution (Borer ChemieAG) for 30 min at 30 °C. Next, the crystals were rinsed with ultrapure water (Hydrolab, conductivity: 0.056 μS cm^{-1}) and kept in water for 2 h. Before seeding the cells, the crystals were rinsed with 99.8% ethanol and dried with a stream of argon.

2.3.7 Metallomics assessment using the LA-ICP-MS method. A quadrupole mass spectrometer with an inductively coupled plasma ionization instrument, ICP-MS, (Nexion 300D, PerkinElmer, USA) was coupled to the 213 nm UV (Nd-YAG, solid state, Q-switched) laser ablation system (LSX-213, CETAC, USA). The laser system parameters and settings were set as follows: wavelength = 213 nm, pulse duration = 5 ns, beam diameter = 100 μm, repetition rate = 10 Hz, carrier gas Ar, and ablation mode = line (n = 6 per sample). ICP MS characteristics and settings were set as follows: RF power = 1400, neb. gas flow rate = 0.99, dwell time = 5 ms, pre-integration time = 20 s, and isotopes monitored: ^{12}C, ^{23}Na, ^{26}Mg, ^{27}Al, ^{31}P, ^{32}S, ^{35}Cl, ^{39}K, ^{43}Ca, ^{55}Mn, ^{57}Fe, ^{66}Zn, and ^{197}Au. For all measurements, the samples remaining from the glycan structure analysis were placed inside the ablation cell. Six lines were ablated at locations covering the middle part of the sample surface. Transient signals were recorded and evaluated for the relative elemental content comparison. The LA-ICP-MS signals were background corrected and integrated using Excel software. All spikes (defined as single data points exceeding the intensities of the neighboring data more than 2 times) were removed automatically using a home-written macro and were replaced with the values of the average of two neighboring signal intensities. The results for all samples were calculated using the signal of Au as the internal standard. All signals were averaged for each sample and the individual isotope, respectively, before comparison of the obtained results. No normalization was applied.

2.4 Magnetic fluid hyperthermia in cell studies

The H22/987 cells plated in a 35 mm-Petri dish (Falcon; Corning, Durham, NC, USA) at a defined density were incubated for 24 h. After 24 h of cell adhesion, the cells were exposed to magnesium-doped iron(III) oxide NPs and further magnetized for 45 minutes with alternative magnetic fields. The magnetization parameters were set as follows: frequency f

= 110.1 kHz, capacitor 200 mF, magnetic induction B = 18 mT (magnetic field strength H_0 = 14.4 kA m^{-1}, current 11.04 A, and voltage 26.92 V) or B = 21 mT (magnetic field strength H_0 = 16.7 kA m^{-1}, current 13.6 A, and voltage 30.4 V). A MagneTherm™ system (nanoTherics™) was used in the studies. The system consists of a CPX400SP 420 W DC power supply, a TG2000 20 MHz DDS function generator, an SDS 1022 DL digital storage oscilloscope and an induction heating coil with 17 turns of 44 mm inner diameter and cut around the inner side of the hollow cylinder. To keep the coil temperature at the ambient temperature (25 °C) or incubator temperature (37 °C), a water circulation unit was provided inside the coil, connecting it to the water jacket using a Grant LT ECOCOOL 150 electronic thermostat system (Grant Instruments Ltd). The increase of sample temperature was measured using a fiber-optic thermometer (Osensa™).

2.5 Magnetic fluid hyperthermia in animal studies

All animal procedures were performed in accordance with the Guidelines for the Care and Use of Laboratory Animals of the Warsaw University of Life Sciences and were approved by the Institutional Animal Ethics Committee of the Warsaw University of Life Sciences (approval no. WAW2/077/2022). Six week-old male NUDE Balb/c mice purchased from Charles River Laboratories (Germany) were housed in a group of five in Individually Ventilated Cages (IVCs) with free access to a standard diet (Altromin) and water *ad libitum*, and they were placed under a 12 h light/dark cycle. The animals were acclimated to the animal facility for at least one week prior to the experimental procedure and were injected into the right flank with 4 × 10^6 H22/987 cells suspended in 100 microliters of the culture medium to generate patient-derived xenograft (PDX) models. Two weeks post-implantation, the naïve mice bearing *ca.* 3–4 mm tumors were injected intratumorally (0.1 mL) with $Mg_{0.1}$-γ-Fe_2O_3(mPEG-silane)$_{0.5}$ NPs (3 mg mL^{-1}) and subjected to an AMF for 30 min. The system used for magnetic fluid hyperthermia consists of a central magnetization unit called magneTherm™ (nanoTherics Ltd), a CPX400SP 420 W DC power supply, a TG2000 20 MHz DDS function generator, an SDS 1022 DL digital storage oscilloscope and an induction heating coil with 17 turns of 44 mm inner diameter and cut around the inner side of the hollow cylinder. To keep the coil temperature at the incubator temperature (37 °C), a water circulation unit was provided inside the coil, connecting it to the water jacket using a Grant LT ECOCOOL 150 electronic thermostat system (Grant Instruments Ltd). The experimental setup for magnetization parameters *in vivo* was as follows: magnetic induction value B = 23 mT, magnetic field strength H_0 = 18.3 kA m^{-1}, frequency f = 110.1 kHz, current = 13.17 A, voltage = 32.0 V, capacitor = 200 mF, and $H \times f$ = 2 × 10^9 A ms^{-1}. The animals were thermally imaged using an infrared (IR) camera (Optrics™) before magnetization and during 5, 10, 15, 20, and 30 min of magnetization, following IR imaging for the next 15 min without magnetic fields (the cooling period). The magnetization of animals was performed four times at weekly intervals. Before each magnetization session, the animals were injected intratumorally (0.1 mL) with NPs (3 mg mL^{-1}). Non-magnetized mice dosed intratumorally with normal saline served as controls. The SAR was calculated based on the initial slope method, following the latest methodological standards.[41–45] All mice were subjected to post-experimental necroscopy and the collected tumours were subjected to histological examination.

2.6 Statistical analysis

At least three independent experiments were conducted for each experimental point in studies. If the results are expressed as the percentage of the untreated control, the statistical evaluation of their significance was done on raw data. Differences were considered statistically significant when the P-value was less than <0.05. The normal distribution of data was confirmed by the Shapiro–Wilk test. In the absence of normality, the homogeneity of variance data was assessed by Kruskal–Wallis one-way analysis of variance on ranks. Significant differences between data were assessed by one-way analysis of variance (ANOVA) and Dunnett's *post hoc* test. Significance was expressed as follows: $^*p < 0.01$, $^{**}0.0011 \leq p \leq 0.0004$, $^{***}p \leq 0.0007$, and $^{****}p \leq 0.0001$ *vs.* control. All statistical analyses were performed using GraphPad Prism 10.4.1 (Dotmatics) and Statistica 13.3 (TIBCO Software Inc.).

3. Results and discussion

Magnesium-doped iron(III) oxide nanoparticles coated with mPEG-silane were recently synthesized and extensively characterized in our laboratories.[22] The NPs were prepared with a defined stoichiometric ratio of $Mg_{0.1}$-γ-Fe_2O_3(mPEG-silane)$_{0.5}$ subsequently characterized through a broad range of physicochemical analyses.[22] A summary of the obtained results is presented in Table S1 of the SI.

Transmission electron microscopy (TEM) revealed uniform, hexagonal and/or rhombohedral nanoparticles with an average diameter of approximately 27 nm (Fig. 2, Fig. S1 and S2). The elemental composition was verified through energy-dispersive X-ray spectroscopy (EDS) and inductively coupled plasma mass spectrometry (ICP-MS), confirming the incorporation of Mg and the presence of Fe and O elements.[22] X-ray diffraction (XRD) analysis confirmed the crystalline phase as γ-Fe_2O_3, with magnesium doping not altering the primary crystal structure[22] (Fig. S3). Fourier-transform infrared (FT-IR) spectroscopy and Raman analysis confirmed successful surface functionalization with mPEG-silane, which contributed to hydrophilicity and stable dispersion in aqueous media[22] (Fig. S4 and S5). The coating ensured colloidal stability of the nanoparticles, making them suitable for biomedical applications. The Mg-doped NPs exhibited soft ferromagnetic behavior, as evidenced by magnetic hysteresis. The saturation magnetization (M_s) reached approximately 70 emu g^{-1}, while the remnant magnetization (M_r) was around 1.6 emu g^{-1} (Fig. S6). These magnetic properties suggest that the nanoparticles are suitable for magnetic field-mediated applications. Under alternating magnetic

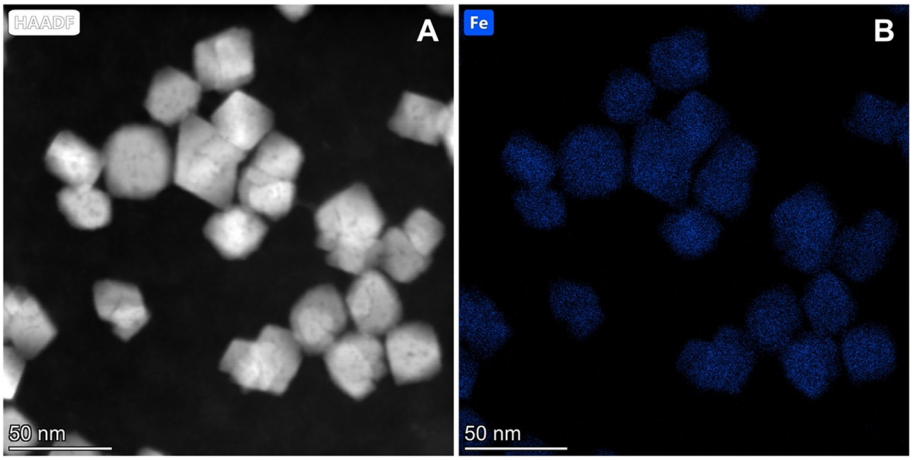

Fig. 2 (A) Representative high-angle annular dark-field (HAADF)-STEM image of iron(III) oxide nanoparticles doped with magnesium ($Mg_{0.1}$-γ-Fe_2O_3(mPEG-silane)$_{0.5}$). (B) Representative (HAADF)-STEM image and energy dispersive X-ray (EDX) map of iron (Fe) elements in $Mg_{0.1}$-γ-Fe_2O_3(mPEG-silane)$_{0.5}$ nanoparticles (please see Nowicka *et al.*[22] for more details).

field conditions, the nanoparticles displayed excellent heating capabilities. A 3.0 mg mL^{-1} dispersion of the ferrofluid reached temperatures exceeding 90 °C within 10 minutes at a field strength of ~18.3 kA m^{-1} and a frequency of 110.1 kHz. In cellular environments (A549 lung cancer cells, 0.25 mg mL^{-1}), the temperature was controlled between 43 and 45 °C, consistent with hyperthermia treatment ranges. SAR values ranged from 429 to 596 W g^{-1}, depending on the analytical model applied (the initial slope, the corrected slope, or the Box–Lucas method)[22] (Table S1). The NPs maintained excellent dispersion stability in aqueous media and exhibited low cytotoxicity in the absence of an AMF. These features confirm their potential as magnetically responsive agents for biomedical applications, particularly in magnetic hyperthermia. We also investigated the *in vitro* biological effects of $Mg_{0.1}$-γ-Fe_2O_3(mPEG-silane)$_{0.5}$ in human lung cells (A549) and normal human bronchial epithelial cells (BEAS-2B). The nanoparticles demonstrated high colloidal stability in cell culture media and were internalized by both cell types, with more efficient uptake observed in the cancer-derived A549 cells. Cytotoxicity assays revealed no reduction in cell viability across tested nanoparticle concentrations and exposure durations in either cell line, indicating favorable biocompatibility. Although a slight increase in intracellular reactive oxygen species (ROS) was detected following nanoparticle exposure, this did not result in measurable DNA strand breaks or oxidative DNA damage, as assessed by genotoxicity assays. Moreover, cell migration assays showed no significant changes in migratory behavior in response to nanoparticle treatment. Collectively, these findings support the less cytotoxic and genotoxic profile of the $Mg_{0.1}$-γ-Fe_2O_3(mPEG-silane)$_{0.5}$ NPs under the tested conditions and suggest their potential suitability for biomedical applications such as MFH[23] (Table S1).

To assess the effects of MFH on a patient-derived lung cancer cell line (H22/987) using $Mg_{0.1}$-γ-Fe_2O_3(mPEG-silane)$_{0.5}$ NPs, we began by examining cell metabolism using the AB assay – a method commonly employed in toxicological studies, as it is considered a reliable test for evaluating cytotoxicity, cell proliferation, and metabolic activity.[46] A summary of the experimental results obtained after the application of MFH on H22/987 cancer cells is shown in Fig. 3A. The results obtained regarding the viability of lung cancer cells following hyperthermic therapy demonstrate a significant decrease in cell population under all tested conditions. The viability of the cells after exposure to 18 mT AMF and NPs showed a surviving fraction of approximately 31–40%, compared to the control value (100%) recorded under standard conditions. Exposure to a higher magnetic induction value of 21 mT resulted in a more pronounced reduction in cell viability, ranging from 12% to 17%. As anticipated, the increase in cell mortality is directly associated with the higher temperature attained during the experiment.[47] To further evaluate the cytotoxic potential of the NPs used for MFH, additional experiments were conducted across a concentration range of 0–250 μg mL^{-1}. A slight cytotoxic effect was observed at concentrations between 100 and 250 μg mL^{-1} only, whereas lower concentrations had no detectable impact on cell viability (data not shown). Given the satisfactory outcome at the level of 37% and considering that any additional increase in temperature may adversely affect the surrounding tissue, the decision was made to utilize a magnetic induction value of 18 mT in the subsequent stages of the study. This step allowed for definitive determination of the magnetic induction value to be employed in further investigations. Since the Alamar Blue assay reflects the reductive environment of metabolically active cells,[37] the obtained results suggest that the MFH process may exert a detrimental effect on the mitochondria of H22/987 cells, leading to metabolic dysfunction.

In this study, the effect of MFH using $Mg_{0.1}$-γ-Fe_2O_3(mPEG-silane)$_{0.5}$ NPs on H22/987 cells was further evaluated using the TB exclusion assay, which assesses potential damage to the cell membrane.[38] The percentages of viable cells were deter-

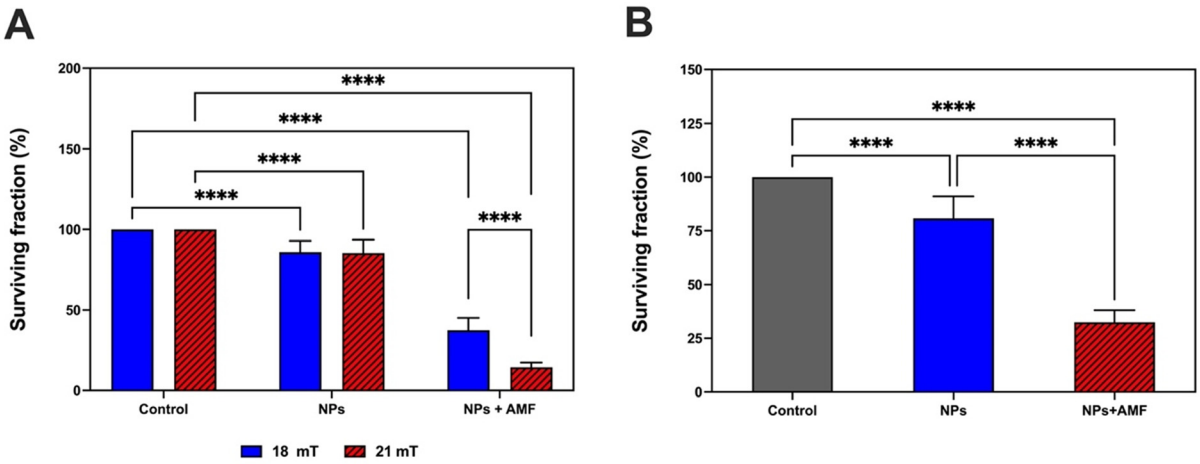

Fig. 3 (A) Cytotoxic effects of $Mg_{0.1}$-γ-Fe_2O_3(mPEG-silane)$_{0.5}$ NPs (250 μg mL^{-1}) on H22/987 cells treated with (NPs + AMF) and without an AMF (NPs) assessed using the Alamar Blue assay between two measurement conditions *i.e.* 18 mT and 21 mT of the magnetic induction value. (B) Cytotoxic effects of $Mg_{0.1}$-γ-Fe_2O_3(mPEG-silane)$_{0.5}$ NPs (250 μg mL^{-1}) on H22/987 cells treated with (NPs + AMF; a magnetic induction value of 18 mT) and without an AMF (NPs) assessed using the Trypan Blue assay.

mined relative to the control cells, with the assumption of 100% viability for the control cell population. The TB assay confirmed the observed morphological effect during treatment with a magnetic induction value of 18 mT, presented in Fig. 3B. The observed reduction in cell survival following treatment with magnetic fields, as assessed by the TB assay, indicates significant membrane permeabilization. It is well established that heat affects plasma membrane proteins, altering membrane permeability. This can result in cell death or enhance the cells' sensitivity to additional stress.[48] In our previous study, we presented TEM images (please see ref. 49) demonstrating that exposure to an AMF resulted in substantial accumulation of NPs both inside and outside the lung cancer cells (A549) after a 24-hour incubation period. In their insightful study, Calatayud *et al.* chose to compare membrane damage induced by water bath hyperthermia with that caused by MFH. Based on TEM and SEM results, they observed significant damage to the cell membrane structure exposed to the NPs and AMF. Conversely, hot-water bath treatment resulted in severe internal cell damage, although some cells retained a relatively intact membrane structure. It has been suggested that an additional mechanism of cell damage is associated with the presence of magnetic NPs within the intracellular space.[50]

An important determinant of therapeutic efficacy is the analysis of migration and invasion of cancer cells, as it constitutes a pivotal step in the metastatic process.[51,52] The biological processes governing cell migration heavily rely on the cell types involved and the surrounding cellular microenvironments.[53] The migration of healthy cells is firmly regulated, whereas conversely, the altered cancer microenvironment promotes excessive cell migration. There are numerous factors influencing the ability of cells to migrate, rendering this process highly complex.[54] In this study, the H22/987 cell migration was assessed after MFH treatment with $Mg_{0.1}$-γ-Fe_2O_3(mPEG-silane)$_{0.5}$ NPs (250 μg mL^{-1}) and a magnetic induction value of 18 mT, using the WH assay.[55] Conversely, non-treated control samples were observed, and the cells were exposed to $Mg_{0.1}$-γ-Fe_2O_3(mPEG-silane)$_{0.5}$ NPs. There is no significant difference between the control cells and cells incubated with NPs or cells after hyperthermia treatment (NPs + AMF) at 24 h, as shown in Fig. 4A, with additional images provided in Fig. 4B. However, we report that the proposed MFH therapy exhibits some effects on lung cancer cell migration, restricting this process at 48 h post-treatment, as assessed by the WH assay. Microscopic analysis clearly demonstrates a reduction in cellular overgrowth in the "scratch" zone relative to the control and hyperthermia groups at 24 hours (Fig. 4B). It should be noted that cell migration is a highly intricate process in which the interactions between cells and the extracellular matrix play a crucial role. The patterns of cell movement within extracellular microenvironments can exhibit significant variability, influenced not solely by the cell type and biochemical composition of the extracellular matrix but also by its physical and mechanical characteristics. Numerous pathways for cell migration within the extracellular matrix have been elucidated by various researchers.[56] Concurrently, reports from other scientists suggest that iron oxide NPs themselves restrict cell migration by inhibiting actin cytoskeleton activity and disrupting microtubule networks. Recently, Nica *et al.* demonstrated results where PC-3 cells responded to hyperthermia in decreased viability,[57] similarly to the A549 cell line in the presence of an external magnetic field and SPION irradiated additionally with visible laser light.[58]

Among the gold-standard methods for evaluating cancer therapy efficacy are clonogenic assays, with the CFE assay being the most prominent, as it measures the ability of individual cancer cells to proliferate and form colonies.[59] In this investigation, the CFE assay was employed to evaluate the proliferation of primary lung cancer cells following treatment with

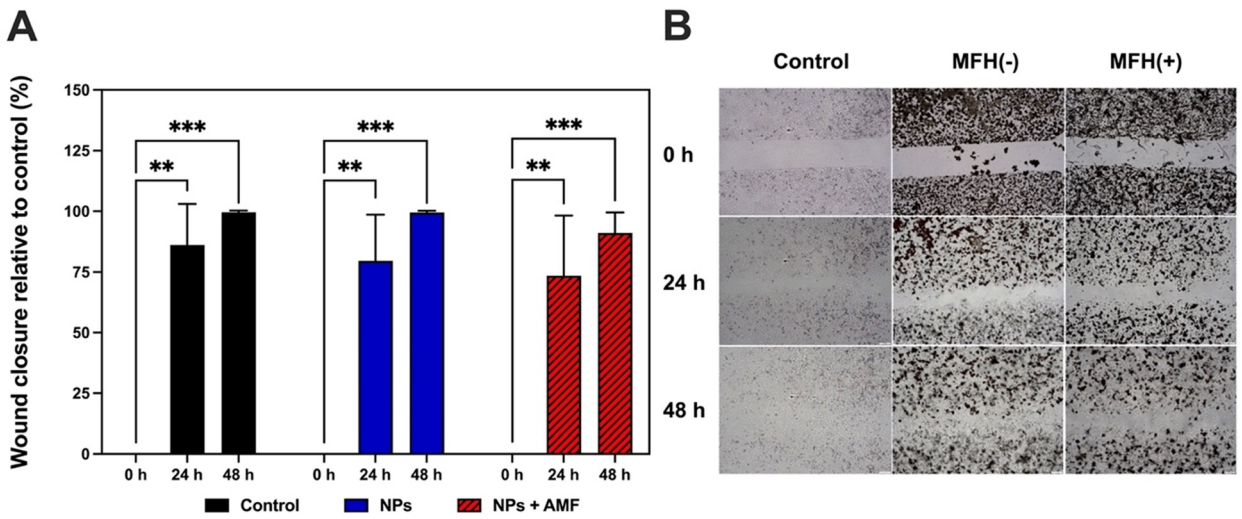

Fig. 4 (A) Percentage of wound closure area plotted over time as determined by the wound healing assay assessed on taken images. An experiment conducted on H22/987 cells using $Mg_{0.1}$-γ-Fe_2O_3(mPEG-silane)$_{0.5}$ NPs (250 μg mL^{-1}) in two models: with (NPs + AMF; a magnetic induction value of 18 mT) and without an AMF (NPs). (B) Representative microscopy images of H22/987 cells from the wound healing assay. Cells were treated with $Mg_{0.1}$-γ-Fe_2O_3(mPEG-silane)$_{0.5}$ nanoparticles with and without MFH. Non-treated H22/987 cells served as controls.

MFH. During the experiments, two doses of $Mg_{0.1}$-γ-Fe_2O_3(mPEG-silane)$_{0.5}$ NPs were tested: 250 μg mL^{-1} and 500 μg mL^{-1}. To evaluate the proliferative potential of individual H22/987 cancer cells, colony formation was assessed 12 days after plating. Before accepting the results, it was ensured that each of the experiments met the acceptance criteria outlined earlier by Kinsner-Ovaskainen *et al.*, including, among other factors, that the cell count in a single colony (non-treated control) should not be less than 50 individual cells.[60] Cell exposure to the NPs and AMF resulted in significant inhibition of cell growth, with a higher concentration of NPs causing complete cell eradication, as presented in Fig. 5A with additional photos in Fig. 5B. A similar effect was observed for the positive control, which involved treating the cells with a 10 μM solution of sodium chromate (0% survival fraction). Concurrently, incubation with NPs alone and with a 10%

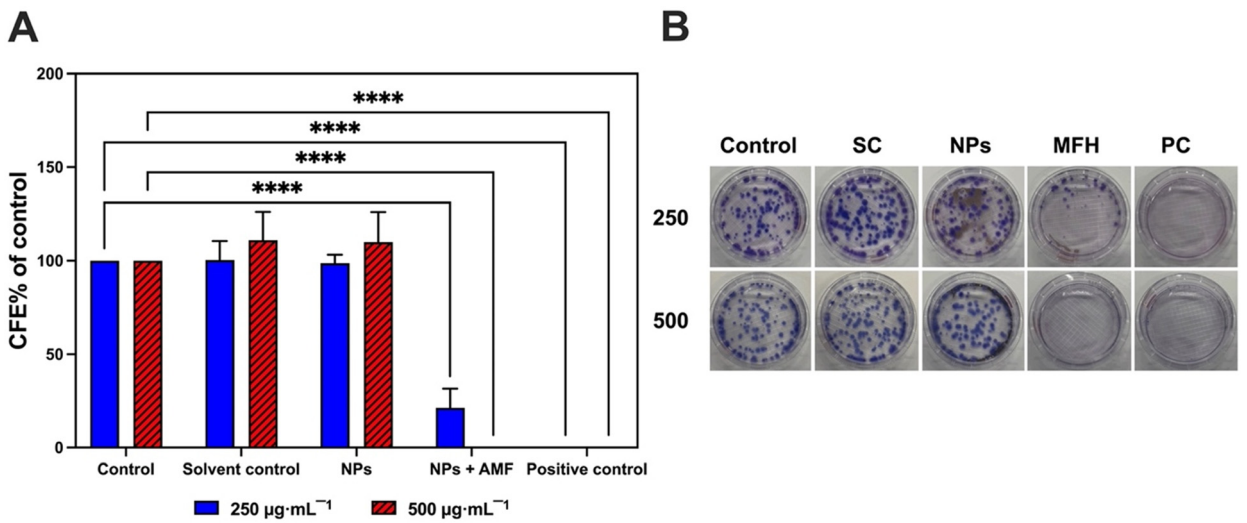

Fig. 5 (A) Cytotoxic effect of $Mg_{0.1}$-γ-Fe_2O_3(mPEG-silane)$_{0.5}$ NPs on H22/987 cells assessed by the Colony Forming Efficiency (CFE) assay. An experiment conducted using $Mg_{0.1}$-γ-Fe_2O_3(mPEG-silane)$_{0.5}$ NPs (250 μg mL^{-1} and 500 μg mL^{-1}) in two models: with (NPs + AMF; a magnetic induction value of 18 mT) and without an AMF (NPs). For the positive control, treatment with 100 μM Na_2CrO_4 was used. The number of colonies is presented as a percentage relative to the number of colonies in the control. (B) Representative microscopy images of H22/987 cells from the CFE assay. The cells were treated with $Mg_{0.1}$-γ-Fe_2O_3(mPEG-silane)$_{0.5}$ nanoparticles with and without an AMF to produce MFH. Nanoparticle concentrations are 250 μg mL^{-1} (top panel) and 500 μg mL^{-1} (bottom panel). Positive control, PC (sodium chromate, Na_2CrO_4, 100 μM), solvent control, SC (ultrapure water) and control (medium). NPs are $Mg_{0.1}$-γ-Fe_2O_3(mPEG-silane)$_{0.5}$ nanoparticles and MFH denotes magnetic fluid hyperthermia.

volume of solvent, which was water, was also examined. At a dose of 500 μg mL^{-1}, a slight increase in the number of colonies was observed both in the case of incubation with the solvent and with the NPs (approximately 117–119%). However, there was no statistical significance compared to the control. The as-obtained results demonstrated the suppressive impact of the administered MFH treatment on tumor cell proliferation, underscored by its notable capability to markedly diminish the cell's capacity for colony formation. The findings from the CFE assay employing two dosages of $Mg_{0.1}$-γ-Fe_2O_3(mPEG-silane)$_{0.5}$ NPs validate the dose-dependent cytotoxicity of the nanomaterials in conjunction with AMF exposure. Such results also suggest potential long-term cytotoxic effects associated with intracellular MFH.

Matrix metalloproteinases (MMPs) play a crucial role in regulating physiological processes and signaling events between tumors and their stroma. MMPs perform various functions under both physiological and pathological conditions. Depending on the conditions, they can either inhibit or promote tumor development. The levels of MMPs are considered promising indicators of tumor progression, inflammation within the tumor microenvironment, and cancer cell metastasis.[61] The expression of MMPs in lung cancer is influenced by several factors. It has been demonstrated that infection and inflammation increase the secretion of MMP-1 in lung tissues, with macrophages serving as the primary source. Macrophages also enhance the expression and secretion of MMP-9 upon immunological stimulation and require its activity for migration during the inflammatory response. Furthermore, pro-inflammatory cytokines are known to play a key role in the release of MMP-1 and MMP-9. Note that MMP activation can also be triggered by ROS. An excellent review of this topic has been conducted by Wei in his study.[62]

In the present study, we focused on analyzing two types of MMPs based on their substrate specificity and cellular localization: MMP-1, representing the group of collagenases, and MMP-2 and MMP-9, which represent the gelatinases. The concentrations of MMP-1, MMP-2, and MMP-9 were analyzed in control samples and after simultaneous exposure to the NPs and AMF. An increase in MMP-1 levels after MFH, compared to the control, was consistently observed regardless of the sample collection method (please refer to Fig. 1A), with the most significant increase occurring after centrifugation, as presented in Fig. 6A. The centrifugation was carried out under standard conditions to avoid stress formation. The levels of MMP-2 and MMP-9 fluctuated between 0.1 and 2.3 compared to the control, regardless of the sample collection method. Following MFH treatment, we observed that non-viable cells detached from the substrate and remained suspended in the culture medium; thus, the analysis of MMPs in these cells corresponds to stages (1) and (2). In this study, the remaining viable cells were detached from the substrate using trypsin, and their MMP profiles are presented in stages (3), (4), and (5). Gentle centrifugation caused the MMP-1 molecules anchored to the cell surface to be released. Although complete cell death was not observed in our study, the surviving cells exhibited structural alterations at multiple levels, which may contribute to delayed cancer progression. It has been demonstrated that MMP-1 collagenases, involved in lung cancer progression, induce cell migration and invasion while reducing proliferation. MMP-1 is also known to regulate the polarization of the Th1/Th2 inflammatory response.[63] In our previous study, we reported significant cell membrane damage and observed vacuolization in A549 cells following MFH treatment.[49] Based on the results obtained in this paper, MFH has been considered to induce extracellular matrix (ECM) degeneration by promoting the production of MMP-1. Interestingly, collagenases are introduced, for example, to enhance drug permeability in pancreatic ductal adenocarcinoma (PDAC). The increase in MMP-1 without a simultaneous increase in MMP-2 and MMP-9 levels may indicate improved membrane permeability, which could be a significant advantage when combining MFH with other therapies.[64]

Additionally, to expand the understanding of the effects of MFH on the H22/987 cells, elemental content analysis was conducted using the LA-ICP-MS method. This technique is gaining increasing popularity among researchers as it enables quantitative determination of trace elements and isotopes in samples with spatial resolution ranging from approximately 10 to 100 μm.[65] As assessed by the LA-ICP-MS method, MFH treatment significantly modulated the metallomics profile in H22/987 cells, as presented in Fig. 6B. MFH treatment notably increased the levels of both iron and magnesium. This elevated content of these elements may primarily result from the presence of NPs themselves, specifically their elemental composition ($Mg_{0.1}$-γ-Fe_2O_3(mPEG-silane)$_{0.5}$). However, in the context of other findings, particularly the increased permeability of the cell membrane, the elevated sodium levels deserve special attention. Sodium levels are regulated by a sodium–potassium pump, which plays a crucial role in maintaining normal cell volume, establishing membrane potential and ion gradients, and facilitating cellular uptake and metabolite release. The increase in sodium concentration following MFH treatment can be attributed both to enhanced plasma membrane fluidity and to a decrease in sodium–potassium pump activity, allowing for increased ion flux.[66,67] Additionally, an increase in calcium levels due to enhanced membrane permeability as a result of hyperthermia has also been reported by other researchers.[68] Of particular interest is the observed change in zinc content relative to control samples, considering that MMPs belong to the family of multidomain Zn-dependent endopeptidases.[69]

Glycans (oligosaccharides) combine with proteins or lipids through the enzymatic process of glycosylation to form glycoproteins and glycolipids, respectively. Among other things, glycans are responsible for the structural stability of proteins, are involved in the incorporation of proteins into cell membranes and their secretion outside the cell, and influence their biological activity.[70] Moreover, glycans play an important role in the process of host–pathogen interaction, as well as the immune response.[71,72] Due to their structural diversity, glycans are involved in many cellular processes, and changes

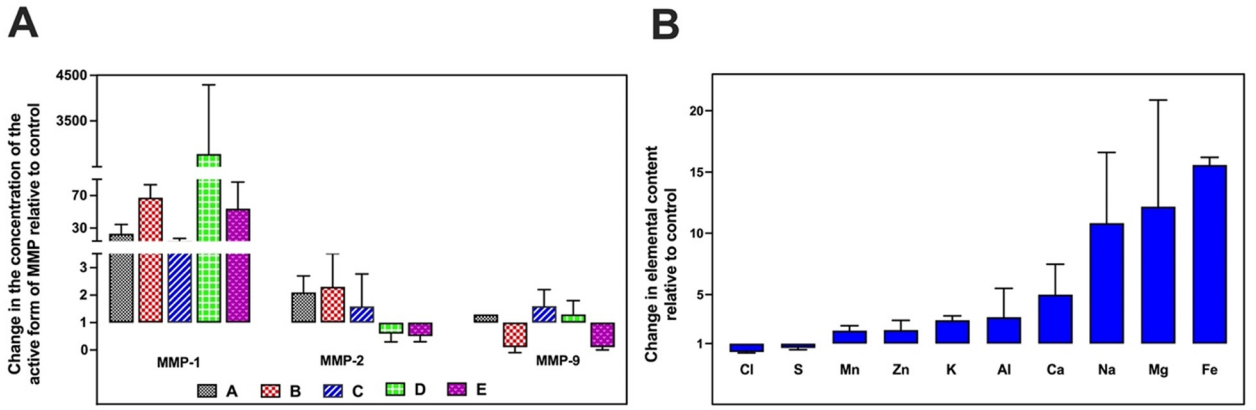

Fig. 6 (A) Results of changes in the concentration of the active form of three metalloproteinases (MMPs) after MFH treatment (250 μg mL^{-1} of $Mg_{0.1}$-γ-Fe_2O_3(mPEG-silane)$_{0.5}$ NPs + AMF; a magnetic induction value of 18 mT) relative to the control. The data are provided for different methods of medium collection (please see Fig. 1A). (B) Results of changes in the elemental content after MFH treatment (250 μg mL^{-1} $Mg_{0.1}$-γ-Fe_2O_3(mPEG-silane)$_{0.5}$ NPs + AMF; a magnetic induction value of 18 mT) on H22/987 cells relative to control samples.

in the glycosylation profile are reflected in adhesion,[73] proliferation,[74] metabolism[75] and cell differentiation,[76] and thus in tumorigenesis. A characteristic feature of tumor cell malignancy is a change in the glycosylation pattern of the cell surface glycocalyx or glycoproteins/glycolipids secreted into body fluids. These changes are the result of genetic mutations associated with tumorigenesis as well as epigenetic changes occurring in the tumor environment. The most commonly observed glycosylation changes in tumor cells include (i) overexpression of *N*-glycans of the β1,6-GlcNAc branching complex type; (ii) overexpression of incomplete *O*-glycans such as T antigen (core 1 *O*-glycans: Galβ1–3GalNAc), Tn antigen (GalNAc) and their sialylated forms (sT and sTn, respectively); (iii) overexpression of sialylated glycans; and (iv) changes in the expression of glycoepitopes of the Lewis group system.[77] These changes may also result from the used cancer therapy.[78,79] One goal of our study was to determine whether MFH alters the glycosylation of tumor cells. In the study, tumor cells from a patient (H22/987) with non-small cell lung cancer were used. To prove our hypothesis, the interaction of tumor cells with concanavalin A (ConA) was performed using a quartz crystal microbalance with dissipation. The obtained results are shown in Fig. 7A. The changes in the frequency shift (Δf) recorded in the real-time interaction of cancer cells (untreated and treated with MFH therapy) with ConA evidently show the difference in the amount of lectin bound to the cells. The Δf changes for hyperthermia-treated cancer cells are more than 2 times smaller with respect to the control (non-hyperthermia-treated cells). This means that more than twice as much ConA was bound to the cells. It should be noted that in the QCM-D technique, a decrease in the frequency shift of a quartz crystal corresponds to an increase in its mass. Lectins interact with glycans at their active site, the so-called carbohydrate recognition domain (CRD), and tend to recognize specific glycan sequences usually consisting of 1–4 sugars. ConA forms hydrogen bonds mainly between the hydroxyl group of the side chain between the terminal α-D-mannosyl and α-D-glucosyl groups[80] and the amide group of CRD residues, mainly asparagine and glutamine.[81] The binding of lectins is non-covalent and includes van der Waals and hydrophobic forces in addition to hydrogen bonds.[82] Taking this fact into account, the obtained QCM-D results indicate that MFH therapy affected the number of interaction sites between glycans and lectin. To obtain more detailed information on the nature of this interaction, the $\Delta D = f(\Delta f)$ relationships shown in Fig. 7B and C were plotted. The presence of two linear ranges on the plotted relationships indicates that ConA interacts differently with the glycans of the analyzed cancer cells. This correlates with the branched structure of the glycans and the different sites of ConA interaction (*via* glucose or mannose). In addition, the ranges differ in slope, which in turn suggests different orientations of ConA molecules interacting with glycans. Treatment of cancer cells with MFH therapy did not affect the number of rectilinear ranges but definitely affected the orientation of glycan-bound ConA molecules (change in the angle of inclination of individual ranges). Smaller differences in the values of the slope angles of the linear ranges of the $\Delta D = f(\Delta f)$ relationship of cells after MFH therapy compared to untreated cells indicate cellular changes. This observation is further supported by results obtained through other methods presented in this paper.

To investigate the impact of MFH using $Mg_{0.1}$-γ-Fe_2O_3(mPEG-silane)$_{0.5}$ *in vivo*, we evaluated experiments in BALB/c nude mice bearing solid lung tumors derived from the H22/987 human lung cancer cells. It should be emphasized that the patient H22/987 was diagnosed based on a comprehensive tomographic (CT) analysis and histological and immunohistological evaluation.[36] This patient underwent removal of the tumor, a fragment of which was used to establish the primary cell line. Transplanting H22/987 cells into the flank of BALB/c nude mice allowed us to set up a patient-derived xenograft (PDX) model. Histological analysis of the H22/987 tumor

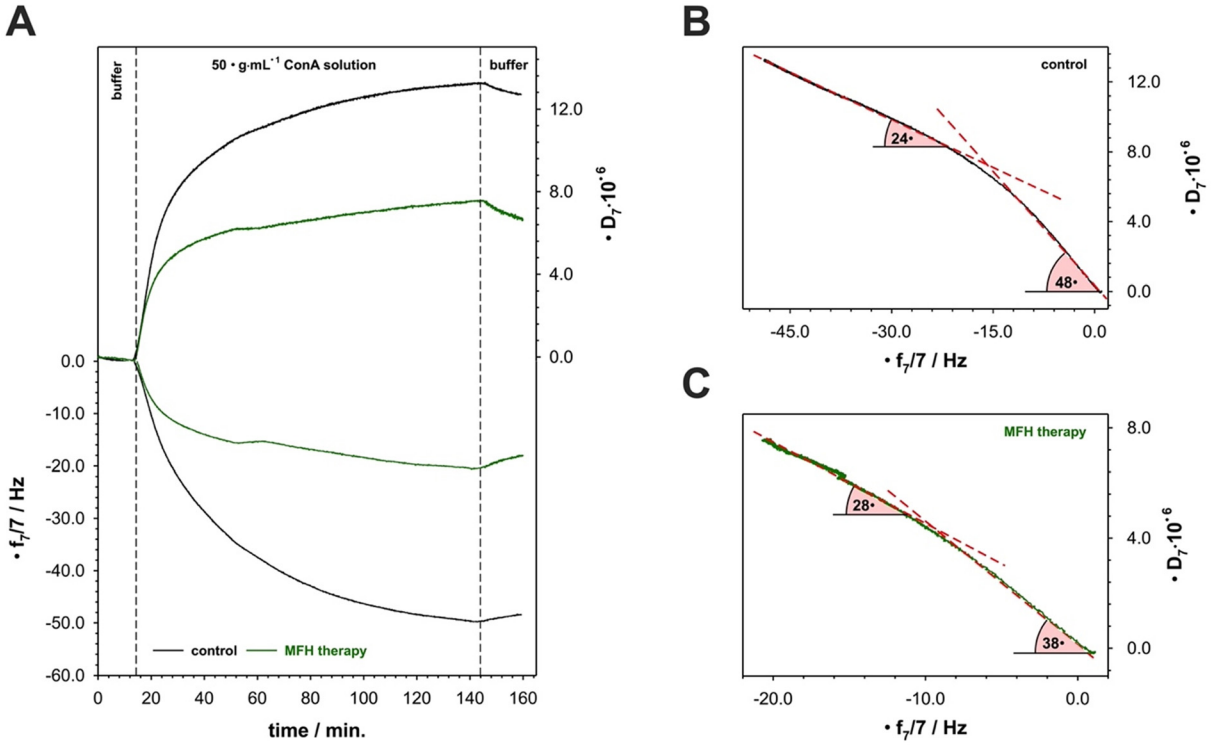

Fig. 7 (A) Typical QCM-D curves of the shifts in frequency (Δf) and dissipation factor (ΔD) during interaction of ConA with H22/987 cells. Dependences $\Delta D = f(\Delta f)$ plotted for H22/987 cells treated (B) without and (C) with MFH. Experimental conditions: C_{ConA} = 50.0 μg mL^{-1}; 0.01 M Gibco buffer with the addition of 0.025% Tween, pH = 7.4, at a flow rate of 25 μL min.$^{-1}$.

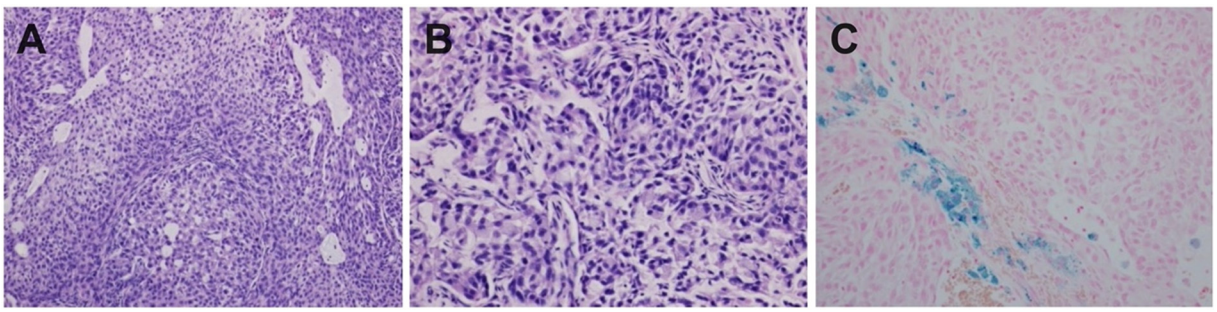

Fig. 8 Representative resection specimens of lung cancer tissues taken from tumors grown as PDX in NUDE BALB/c mice, where (A) control (non-treated) mice (H&E staining, mag. ×100), (B) MFH-treated mice (H&E staining, mag. ×100), and (C) MFH-treated mice (tissues stained with Perls' Prussian Blue for iron, Fe). Numerous iron deposits are visible as blue stains, indicating nanoparticle accumulation.

growing in mice confirmed the type of adenocarcinoma exhibiting glandular (approx. 60%) and mucinous (approx. 40%) types with grades G2 and G3 (Fig. 8A–C).

Prior to each magnetization session, the mice were intratumorally injected with a single dose of magnesium-doped iron(III) oxide NPs ($Mg_{0.1}$-γ-Fe_2O_3(mPEG-silane)$_{0.5}$) and then exposed to an AMF. Following established protocols for MFH used in clinical studies with human subjects,[83] we performed four separate magnetization sessions, each separated by a seven-day interval. The first MFH session was conducted on day 28 after implantation of the lung cancer cells into the right flank of the mice, ensuring a consistent tumor size across all subjects (131.2 ± 77.8 mm^3 in the control group *vs.* 139.2 ± 39.5 mm^3 in the AMF-treated group, $p < 0.05$). Both the treated and untreated groups were regularly monitored for general health, including body weight gain and tumor size (Fig. 9A and C). Control mice not receiving MFH showed significantly faster body weight gain compared to the hyperthermia-treated group (Fig. 9A). Additionally, tumor volumes in the control group increased more rapidly, reaching the critical size threshold that necessitated removal from the study (Fig. 9B). According to animal welfare guidelines, any mice with tumors exceeding 12 mm in at least one direction were excluded from the experiment. As a result, one control mouse was excluded

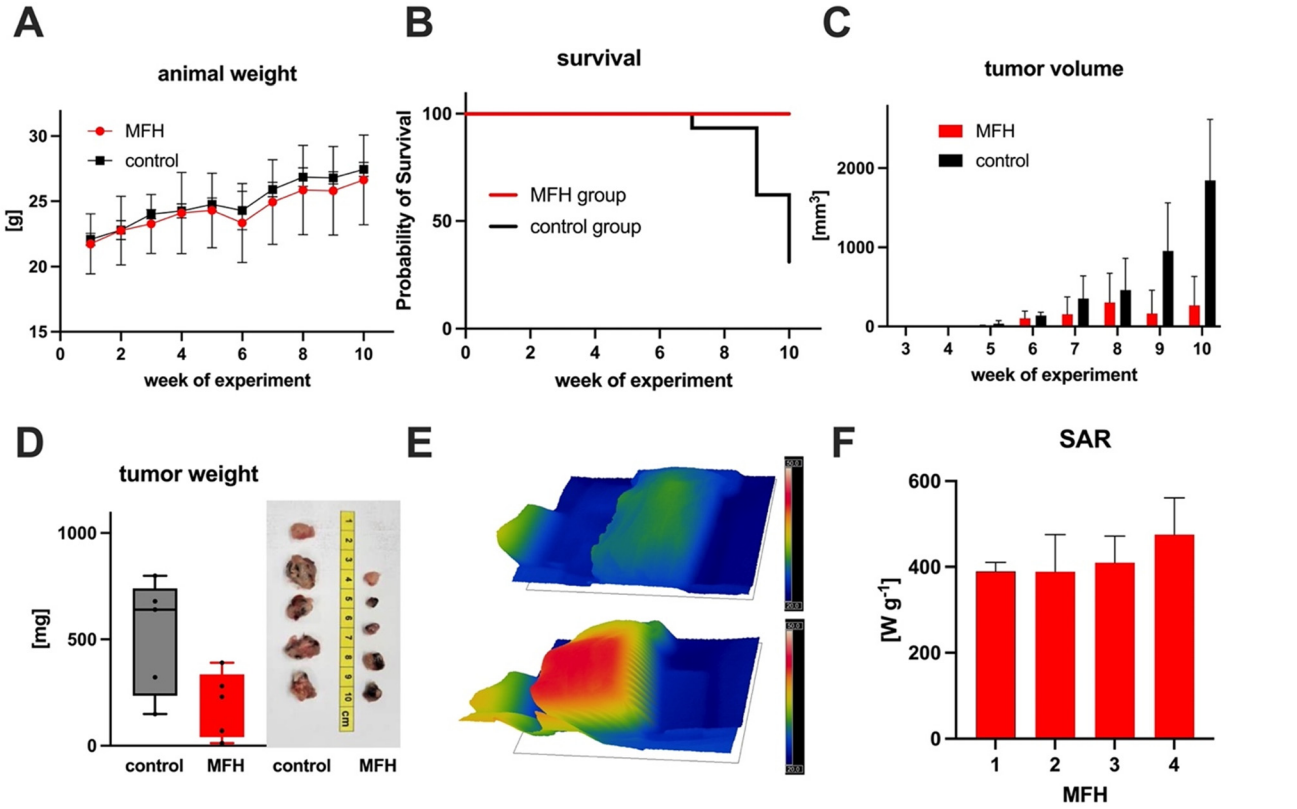

Fig. 9 The therapeutic effectiveness of magnetic fluid hyperthermia evaluated in patient-derived human lung cancer xenografts using NUDE Balb/c mice treated with magnesium-doped iron(III) oxide nanoparticles ($Mg_{0.1}$-γ-Fe_2O_3 (mPEG-silane)$_{0.5}$, 3 mg mL^{-1}) and subjected to an alternating magnetic field (AMF) for 30 min (B = 23 mT, H_0 = 18.3 kA m^{-1}, f = 110.10 kHz, and a capacitor of 200 mF). (A) Changes in the animal body weight throughout the experiment, (B) Kaplan–Meier survival analysis, (C) tumor volume measurements taken on specific treatment days, (D) tumor mass along with representative photographs of lung tumors collected post-mortem from mice at the time of exclusion from the study, (E) representative infrared images showing the temperature distribution among the lung tumor prior to MFH (top panel) and 20 minutes after MFH (bottom panel), and (F) specific absorption rate (SAR) values expressed as mean ± SD (n = 5) for the xenograft model.

on week 7, two on week 9, and one on week 10, whereas no mice in the MFH-treated group were excluded throughout the study (Fig. 9B), and no mortality was recorded in this group. The experiment concluded one week after the final MFH session. Our findings revealed that MFH-treated mice experienced a significant reduction in tumor growth (334.6 ± 365.6 mm^3, $p < 0.05$) when compared to the control group (1845.4 ± 732.1 mm^3, $p < 0.05$) (Fig. 9C). Representative photographs of tumors removed from each group are presented in Fig. 9D, showing that the tumors in the MFH-treated mice exhibited slower growth throughout the study period (196 ± 155 mg *vs.* 518 ± 272 mg, $p < 0.05$). These results suggest that the thermal effects induced by MFH contributed to a marked reduction in tumor size in the treated animals. Interestingly, we showed that the lung cancer growing in mice after MFH treatment has fewer division figures (Fig. 8B). There were also numerous iron deposits in tumor tissues collected from mice bearing PDXs and subjected to MFH (Fig. 8C). In the MFH studies, infrared (IR) imaging was employed with a thermal IR camera to assess the temperature profile of the tumor in magnetized mice (Fig. 9E). Upon injecting NPs into the mice and subjecting them to an AMF, the temperature at the tumor site increased to approximately 43–45 °C.

In general, the generation of heat by nanoparticles is characterized by a parameter known as the specific absorption rate (SAR).[84] Note that NPs with a high SAR are widely favored in cancer therapy due to their ability to minimize patient nanoparticle exposure, employing short periods of exposure to the magnetic field while still achieving the temperature increase necessary to induce cell death.[85] Achieving a high SAR in *in vivo* studies has direct implications for effectively reducing the tumor size.[42] Despite many studies discussing the SAR coefficient, its usage still entails some errors, but to date, no better parameter has emerged to replace it.[44,86] The SAR values derived from *in vivo* studies, calculated using the tumor temperature recorded during each hyperthermia session, ranged between 389 and 475 W g^{-1}, as shown in Fig. 9F. The data underline the exceptional heating efficiency of magnesium-doped iron(III) oxide NPs under *in vivo* conditions, provided that the local nanoparticle concentration is sufficient to achieve the required SAR values within the tumor. By analyzing the temperature profiles within the tumor tissue,

it becomes possible to determine whether the thermal thresholds necessary for tissue injury are reached and maintained over a sufficient duration (Fig. S7–S11). To evaluate the potential of MFH for cancer treatment under conditions of prolonged low-level thermal exposure, the cumulative thermal exposure method was applied as described by *e.g.* Dewhirst *et al.*[87] This method defines an RCEM value of 0.25 for temperatures below 43.0 °C and 0.5 for temperatures above 43.0 °C. Based on this approach, the average cumulative equivalent minutes at 43 °C (CEM43) for all MFH sessions performed on mice with patient-derived human lung adenocarcinoma was calculated to be 9.1 minutes, as derived from the relevant literature.[49] According to van Rhoon *et al.*[88] the minimum thermal dose required to cause tissue damage in mice is 3.4 CEM43. The literature suggests that increasing tissue temperatures to 39–40 °C can enhance blood flow and microcirculation within tumors. As the temperature increases beyond this range, tumor perfusion increases until a critical thermal dose is reached, after which tumor blood flow decreases. Additionally, it has been observed that a temperature threshold of 39 °C promotes nanoparticle extravasation, while temperatures between 40 and 42 °C are linked to enhanced nanoparticle penetration into the tumor.[89,90] The average CEM43 value obtained in this preclinical study on lung cancer exceeds the threshold associated with tissue damage in mice.

4. Conclusions

We have undertaken comprehensive studies aiming to assess the effects of MFH on patient-derived lung cancer cells in alternative (*in vitro*) and murine (*in vivo*) xenograft models using a variety of cytotoxicity assays and mechanistic approaches targeting different cellular and extracellular endpoints. Based on the obtained results, we sought to articulate our hypotheses concerning the structural and overall biochemical differences observed in lung cancer cells subjected to MFH therapy, as illustrated in Fig. 10.

Summarizing the results of the MFH experiments utilizing $Mg_{0.1}$-γ-Fe_2O_3(mPEG-silane)$_{0.5}$ nanoparticles, we demonstrated that this thermal therapy induced some metabolic dysfunctions in lung cancer cells, thereby reducing their proliferation. The ability of these cells to form colonies was markedly diminished and mitochondrial activity was affected. We also observed a significant reduction in lung cancer cell migration, especially at 48 h post-MFH exposure. A noteworthy observation includes the substantial release of matrix metalloproteinases, mainly MMP-1, alterations in metallomic profiles and changes in membrane glycan structures. Based on our findings, it can be inferred that the primary cytotoxic effect of MFH on lung cancer cells is addressed to both the cell membrane and cell–extracellular matrix environment. Importantly, the as-synthesized magnesium-doped iron(III) oxide nanoparticles did not affect the cell membranes of either lung cancerous or noncancerous cells when used alone without applying MFH.[23] The appropriate operation of the plasma membrane, especially regarding its permeability and transport mechanisms, is crucial for the survival and functionality of living cells. The permeability of lung cancer cells increased, as evidenced by the observed exchange of metallic elements between the cells and the medium, the detachment of metalloproteinases and alterations in glycan structures. Collectively, these effects significantly disrupted the proliferation of lung cancer cells, ultimately reducing their numbers and yielding a satisfactory therapeutic outcome. It should be noted that the as-synthesized magnetic nanoparticles used in this study exhibited favorable SAR and CEM43 values, consistent with those reported in the literature. We believe that our work enriches the understanding of cell death mechanisms in human lung cancer following MFH treatments and holds promise for advancing this therapeutic approach in personalized oncology.

Magnesium-doped iron(III) oxide NPs employed in MFH for oncological applications constitute a promising class of nanomedicine-based therapeutic systems, while simultaneously posing distinct regulatory and safety challenges. Depending on their primary mode of action, MFH platforms may be regulated as medicinal products, medical devices, or combination products.[91] Regulatory authorities, including the European Medicines Agency (EMA) and the U.S. Food and Drug Administration (FDA), acknowledge that nanoscale properties can substantially influence biological interactions, tumor selectivity, and safety profiles, thereby requiring a case-by-case, risk-based assessment. Preclinical safety evaluation in the oncological context is centered on detailed physicochemical characterization of iron oxide NPs, including size distribution, magnetic properties, surface chemistry, and stability, which are critical determinants of tumor accumulation and heating efficiency.[92] While *in vitro* studies provide initial insights into cytotoxicity and heat-mediated tumor cell responses, preclinical *in vivo* studies are indispensable, as they enable assessment of tumor retention, off-target biodistribution, accumulation in organs of the mononuclear phagocyte system, clearance pathways, and acute as well as repeat-dose toxicity. These investigations, conducted in accordance with respective ICH guidelines, are essential for defining clinically relevant dose ranges and exposure scenarios in cancer patients. The clinical development of MFH-based oncological therapies follows Good Clinical Practice (GCP) and typically progresses through phases I–III, with a primary focus on the safety, tolerability, and feasibility of tumor-localized heating.[93,94] Particular attention is given to immunological effects, organ accumulation of nanoparticles, and risks associated with repeated treatment cycles. Collectively, current regulatory and scientific consensus indicates that successful clinical translation of MFH in oncology requires integration of rigorous nanoparticle characterization, robust preclinical *in vivo* safety data, and carefully designed clinical trials to demonstrate a favorable benefit–risk profile. The lack of dedicated *in vivo* toxicological studies of the NPs used in MFH represents an important limitation of this work. Although the therapeutic efficacy of MFH was demonstrated, the long-term safety, biodistribution, metabolism, and potential accumulation of nanoparticles in organs cannot be fully assessed. Consequently, the risk of adverse effects or sys-

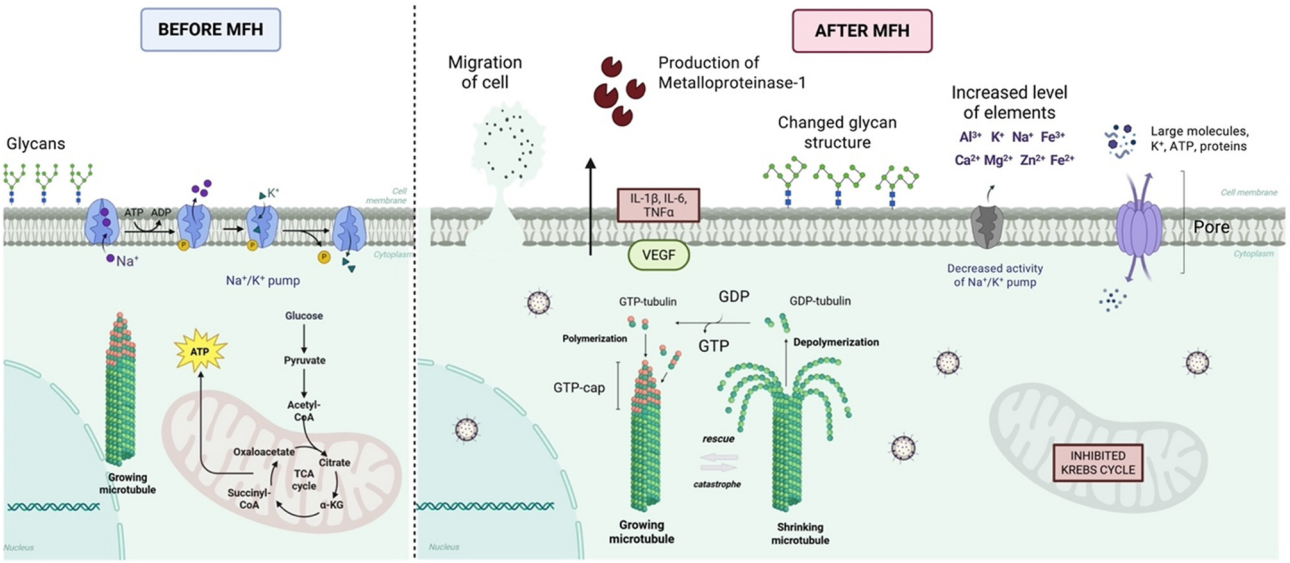

Fig. 10 A schematic representation illustrating the proposed structural and general biochemical changes based on the results presented in this paper. The left side (before MFH) depicts the typical functioning of a cancer cell prior to MFH therapy: properly operating cellular metabolism within the mitochondria (including an intact Krebs cycle) and a correctly functioning sodium–potassium pump on the cell membrane. The right side (after MFH) presents the presumed alterations induced by the therapy, with schematic indications of residual nanoparticles (small spheres within the cell): mitochondrial metabolism appears to be inhibited (and consequently the Krebs cycle is also suppressed). The therapy also seems to affect the cellular membrane activity of the sodium–potassium pump is impaired; pores emerge within the membrane and an increased efflux of elements such as aluminum and potassium from the cell is observed. Additionally, the structure of glycans is disrupted, exhibiting clear changes compared with the pre-MFH state. The therapy appears to influence the cytoskeleton as well, symbolically depicted in the schematic as microtubule contraction.

temic toxicity remains unclear. Further *in vivo* studies specifically focused on toxicological evaluation are required before potential clinical translation can be considered.

Author contributions

Conceptualization: MS and IPG; methodology: MS, IPG, MB-K, MR-A, AMN, and AK; formal analysis: MS, IPG, MB-K, MR-A, AMN, and AK; investigation: MS, IPG, MB-K, MR-A, AMN, AK, AK, GD, BW, MP-S, MC, AS-C, MG, and AC; data curation: MS and IPG; writing – original draft preparation: MS and IPG; writing – review and editing: MS, IPG, MB-K, AMN, and AK; visualization: MS and MB-K; project administration: IPG; funding acquisition: IPG; and supervision: IPG. All authors have read and agreed to the published version of the manuscript.

Conflicts of interest

There are no conflicts to declare.

Data availability

All the data are available and reported in the article. Raw data that support the findings of this study are available from the corresponding author upon reasonable request.

Supplementary information (SI) is available. See DOI: https://doi.org/10.1039/d5nr05036g.

Acknowledgements

This work was financially supported by the programme "Applied Research" through the TEPCAN project granted under the Norwegian Financial Mechanisms 2014–2021/POLNOR 2019 (EEA and Norway Grants), thematic areas: welfare, health and care (NCBR Funding No. NOR/POLNOR/TEPCAN/0057/2019-00). The graphical abstract and Fig. 10 were created using BioRender™ (academic license agreement).

References

1 N. B. Hornback, Historical aspects of hyperthermia in cancer therapy, *Radiol. Clin. North Am.*, 1989, **27**, 481–488.
2 Z. Behrouzkia, Z. Joveini, B. Keshavarzi, N. Eyvazzadeh and R. Z. Aghdam, Hyperthermia: How Can It Be Used?, *Oman Med. J.*, 2016, **31**, 89–97.
3 X. Tang, F. Cao, W. Ma, Y. Tang, B. Aljahdali, M. Alasir and S. Dibart, Cancer cells resist hyperthermia due to its obstructed activation of caspase 3, *Rep. Pract. Oncol. Radiother.*, 2020, **25**, 323–326.
4 S. Lukácsi, G. Munkácsy and B. Győrffy, Harnessing Hyperthermia: Molecular, Cellular, and Immunological

Insights for Enhanced Anticancer Therapies, *Integr. Cancer Ther.*, 2024, **23**, 15347354241242094.
5 T. Iba, Y. Kondo, C. L. Maier, J. Helms, R. Ferrer and J. H. Levy, Impact of hyper- and hypothermia on cellular and whole-body physiology, *J. Intensive Care*, 2025, **13**, 4.
6 K. Richter, M. Haslbeck and J. Buchner, The Heat Shock Response: Life on the Verge of Death, *Mol. Cell*, 2010, **40**, 253–266.
7 K. Ahmed, S. F. Zaidi, M. R. Mati-Ur-Rehman and T. Kondo, Hyperthermia and protein homeostasis: Cytoprotection and cell death, *J. Therm. Biol.*, 2020, **91**, 102615.
8 A. Pawlik, J. M. Nowak, D. Grzanka, L. Gackowska, J. Michalkiewicz and A. Grzanka, Hyperthermia induces cytoskeletal alterations and mitotic catastrophe in p53-deficient H1299 lung cancer cells, *Acta Histochem.*, 2013, **115**, 8–15.
9 D. Toivola, P. Strnad, A. Habtezion and M. Omary, Intermediate filaments take the heat as stress proteins, *Trends Cell Biol.*, 2010, **20**, 79–91.
10 W.-Y. Xie, X.-D. Zhou, J. Yang, L.-X. Chen and D.-H. Ran, Inhibition of autophagy enhances heat-induced apoptosis in human non-small cell lung cancer cells through ER stress pathways, *Arch. Biochem. Biophys.*, 2016, **607**, 55–66.
11 S. K. Calderwood, M. A. Stevenson and G. M. Hahn, Effects of heat on cell calcium and inositol lipid metabolism, *Radiat. Res.*, 1988, **113**, 414–425.
12 R. B. Mikkelsen and T. Stedman, Cytotoxic hyperthermia and Ca2+ homeostasis: The effect of heat on Ca2+ uptake by nonmitochondrial intracellular Ca2+ stores, *Radiat. Res.*, 1990, **123**, 82–86.
13 E. M. Scutigliani, Y. Liang, H. Crezee, R. Kanaar and P. M. Krawczyk, Modulating the Heat Stress Response to Improve Hyperthermia-Based Anticancer Treatments, *Cancers*, 2021, **13**, 1243.
14 A. Deezagi, S. Manteghi, P. Khosravani, N. Vaseli-Hagh and Z.-S. Soheili, Induced apoptosis by mild hyperthermia occurs via telomerase inhibition on the three human myeloid leukemia cell lines: TF-1, K562, and HL-60, *Leuk. Lymphoma*, 2009, **50**, 1519–1527.
15 E. D. Borkamo, O. Dahl, O. Bruland and Ø. Fluge, Global gene expression analyses reveal changes in biological processes after hyperthermia in a rat glioma model, *Int. J. Hyperthermia*, 2008, **24**, 425–441.
16 G. Y. Yi, M. J. Kim, H. I. Kim, J. Park and S. H. Baek, Hyperthermia Treatment as a Promising Anti-Cancer Strategy: Therapeutic Targets, Perspective Mechanisms and Synergistic Combinations in Experimental Approaches, *Antioxidants*, 2022, **11**, 625.
17 P. Das, M. Colombo and D. Prosperi, Recent advances in magnetic fluid hyperthermia for cancer therapy, *Colloids Surf., B*, 2019, **174**, 42–55.
18 H. Fatima, T. Charinpanitkul and K. S. Kim, Fundamentals to Apply Magnetic Nanoparticles for Hyperthermia Therapy, *Nanomaterials*, 2021, **11**, 1203.
19 V. Vijayan, A. Sundaram, A. Vasukutty, R. Bardhan, S. Uthaman and I.-K. Park, Tumor-targeting cell membrane-coated nanorings for magnetic-hyperthermia-induced tumor ablation, *Biomater. Sci.*, 2023, **11**, 7188–7202.
20 J. Idiago-López, D. Ferreira, L. Asín, M. Moros, I. Armenia, V. Grazú, A. R. Fernandes, J. M. de la Fuente, P. V. Baptista and R. M. Fratila, Membrane-localized magnetic hyperthermia promotes intracellular delivery of cell-impermeant probes, *Nanoscale*, 2024, **16**, 15176–15195.
21 P. Das, L. Salvioni, M. Malatesta, F. Vurro, S. Mannucci, M. Gerosa, M. Antonietta Rizzuto, C. Tullio, A. Degrassi, M. Colombo, A. M. Ferretti, A. Ponti, L. Calderan and D. Prosperi, Colloidal polymer-coated Zn-doped iron oxide nanoparticles with high relaxivity and specific absorption rate for efficient magnetic resonance imaging and magnetic hyperthermia, *J. Colloid Interface Sci.*, 2020, **579**, 186–194.
22 A. M. Nowicka, M. Ruzycka-Ayoush, A. Kasprzak, A. Kowalczyk, M. Bamburowicz-Klimkowska, M. Sikorska, K. Sobczak, M. Donten, A. Ruszczynska, J. Nowakowska and I. P. Grudzinski, Application of biocompatible and ultrastable superparamagnetic iron(iii) oxide nanoparticles doped with magnesium for efficient magnetic fluid hyperthermia in lung cancer cells, *J. Mater. Chem. B*, 2023, **11**, 4028–4041.
23 M. Sikorska, M. Ruzycka-Ayoush, I. Rios-Mondragon, E. M. Longhin, S. Meczynska-Wielgosz, M. Wojewodzka, A. Kowalczyk, A. Kasprzak, J. Nowakowska, K. Sobczak, M. Muszynska, M. R. Cimpan, E. Runden-Pran, S. Shaposhnikov, M. Kruszewski, M. Dusinska, A. M. Nowicka and I. P. Grudzinski, Lack of cytotoxic and genotoxic effects of mPEG-silane coated iron(III) oxide nanoparticles doped with magnesium despite cellular uptake in cancerous and noncancerous lung cells, *Toxicol. in Vitro*, 2024, **99**, 105850.
24 X. Liu, Y. Zhang, Y. Wang, W. Zhu, G. Li, X. Ma, Y. Zhang, S. Chen, S. Tiwari, K. Shi, S. Zhang, H. M. Fan, Y. X. Zhao and X. J. Liang, Comprehensive understanding of magnetic hyperthermia for improving antitumor therapeutic efficacy, *Theranostics*, 2020, **10**, 3793–3815.
25 L. Xiong, B. Liang and K. Yu, Magnetic hyperthermia in oncology: Nanomaterials-driven combinatorial strategies for synergistic therapeutic gains, *Mater. Today Bio*, 2025, **33**, 102070.
26 S. Kwon, S. Jung and S. H. Baek, Combination Therapy of Radiation and Hyperthermia, Focusing on the Synergistic Anti-Cancer Effects and Research Trends, *Antioxidants*, 2023, **12**, 924.
27 R. Geoghegan, G. ter Haar, K. Nightingale, L. Marks and S. Natarajan, Methods of monitoring thermal ablation of soft tissue tumors – A comprehensive review, *Med. Phys.*, 2022, **49**, 769–791.
28 C. Brace, Thermal tumor ablation in clinical use, *IEEE Pulse*, 2011, **2**, 28–38.

29 Y. F. Zhang and M. Lu, Advances in magnetic induction hyperthermia, *Front. Bioeng. Biotechnol.*, 2024, **12**, 1432189.
30 H. P. Kok, E. N. K. Cressman, W. Ceelen, C. L. Brace, R. Ivkov, H. Grüll, G. Ter Haar, P. Wust and J. Crezee, Heating technology for malignant tumors: a review, *Int. J. Hyperthermia*, 2020, **37**, 711–741.
31 D. Egea-Benavente, J. G. Ovejero, M. D. P. Morales and D. F. Barber, Understanding MNPs Behaviour in Response to AMF in Biological Milieus and the Effects at the Cellular Level: Implications for a Rational Design That Drives Magnetic Hyperthermia Therapy toward Clinical Implementation, *Cancers*, 2021, **13**, 4583.
32 J. Wu, Z. Zhou, Y. Huang, X. Deng, S. Zheng, S. He, G. Huang, B. Hu, M. Shi, W. Liao and N. Huang, Radiofrequency ablation: mechanisms and clinical applications, *MedComm*, 2024, **5**, e746.
33 F. Dong, Y. Wu, W. Li, X. Li, J. Zhou, B. Wang and M. Chen, Advancements in microwave ablation for tumor treatment and future directions, *iScience*, 2025, **28**, 112175.
34 M. P. Seaton, J. C. Schmidt, N. J. Brown, R. Sahyouni, A. A. Khalessi, S. Ben-Haim and D. D. Gonda, Contemporary Applications of Laser Interstitial Thermal Therapy: A Comprehensive Systematic Review, *World Neurosurg.*, 2025, **193**, 356–372.
35 R. Yao, J. Hu, W. Zhao, Y. Cheng and C. Feng, A review of high-intensity focused ultrasound as a novel and non-invasive interventional radiology technique, *J. Interventional Med.*, 2022, **5**, 127–132.
36 M. Ruzycka-Ayoush, M. Prochorec-Sobieszek, A. Cieszanowski, M. Glogowski, A. Szumera-Cieckiewicz, J. Podgorska, A. Targonska, K. Sobczak, G. Mosieniak and I. P. Grudzinski, Extracellular Vesicles as Next-Generation Biomarkers in Lung Cancer Patients: A Case Report on Adenocarcinoma and Squamous Cell Carcinoma, *Life*, 2024, **14**, 408.
37 S. N. Rampersad, Multiple Applications of Alamar Blue as an Indicator of Metabolic Function and Cellular Health in Cell Viability Bioassays, *Sensors*, 2012, **12**, 12347–12360.
38 W. Strober, Trypan Blue Exclusion Test of Cell Viability, *Curr. Protoc. Immunol.*, 2015, **111**, A3.B.1–A3.B.3.
39 C.-C. Liang, A. Y. Park and J.-L. Guan, In vitro scratch assay: a convenient and inexpensive method for analysis of cell migration in vitro, *Nat. Protoc.*, 2007, **2**, 329–333.
40 K. Winkler, A. Kowalczyk, P. Bereza, K. Regulska, A. Kasprzak, M. Bamburowicz-Klimkowska and A. M. Nowicka, Levels of active forms of MMP-1, MMP-2, and MMP-9 as independent prognostic factors for differentiating the stage and type of lung cancer (SCLC and NSCLC), *Sens. Actuators, B*, 2024, **406**, 135421.
41 V. Darvishi, M. Navidbakhsh and S. Amanpour, Heat and mass transfer in the hyperthermia cancer treatment by magnetic nanoparticles, *Heat Mass Transfer*, 2022, **58**, 1029–1039.
42 R. Hergt, S. Dutz, R. Müller and M. Zeisberger, Magnetic particle hyperthermia: nanoparticle magnetism and materials development for cancer therapy, *J. Phys.: Condens. Matter*, 2006, **18**, S2919.
43 G. Vallejo-Fernandez, O. Whear, A. G. Roca, S. Hussain, J. Timmis, V. Patel and K. O'Grady, Mechanism of hyperthermia in magnetic nanoparticles, *J. Phys. D: Appl. Phys.*, 2013, **46**, 312001.
44 A. A. El-Gendy, E. M. M. Ibrahim, V. O. Khavrus, Y. Krupskaya, S. Hampel, A. Leonhardt, B. Büchner and R. Klingeler, The synthesis of carbon coated Fe, Co and Ni nanoparticles and an examination of their magnetic properties, *Carbon*, 2009, **47**, 2821–2828.
45 M. Harabech, J. Leliaert, A. Coene, G. Crevecoeur, D. Van Roost and L. Dupré, The effect of the magnetic nanoparticle's size dependence of the relaxation time constant on the specific loss power of magnetic nanoparticle hyperthermia, *J. Magn. Magn. Mater.*, 2017, **426**, 206–210.
46 E. M. Longhin, N. El Yamani, E. Rundén-Pran and M. Dusinska, The alamar blue assay in the context of safety testing of nanomaterials, *Front. Toxicol.*, 2022, **4**, 981701.
47 R. Haghniaz, R. D. Umrani and K. M. Paknikar, Temperature-dependent and time-dependent effects of hyperthermia mediated by dextran-coated La0.7Sr0.3MnO3: in vitro studies, *Int. J. Nanomed.*, 2015, **10**, 1609–1623.
48 J. Verma, S. Lal and C. J. F. Van Noorden, Nanoparticles for hyperthermic therapy: synthesis strategies and applications in glioblastoma, *Int. J. Nanomed.*, 2014, **9**, 2863–2877.
49 M. Sikorska, G. Domanski, M. Bamburowicz-Klimkowska, A. Kasprzak, A. M. Nowicka, M. Ruzycka-Ayoush and I. P. Grudzinski, Studies on the thermal sensitivity of lung cancer cells exposed to an alternating magnetic field and magnesium-doped maghemite nanoparticles, *Cancer Nanotechnol.*, 2024, **15**, 38.
50 M. P. Calatayud, E. Soler, T. E. Torres, E. Campos-Gonzalez, C. Junquera, M. R. Ibarra and G. F. Goya, Cell damage produced by magnetic fluid hyperthermia on microglial BV2 cells, *Sci. Rep.*, 2017, **7**, 8627.
51 S. Gerstberger, Q. Jiang and K. Ganesh, Metastasis, *Cell*, 2023, **186**, 1564–1579.
52 J. Fares, M. Y. Fares, H. H. Khachfe, H. A. Salhab and Y. Fares, Molecular principles of metastasis: a hallmark of cancer revisited, *Signal Transduction Targeted Ther.*, 2020, **5**, 28.
53 D. Wu and F. Lin, in *Comprehensive Biotechnology (Third Edition)*, ed. M. Moo-Young, Pergamon, Oxford, 2011, pp. 521–528.
54 F. Merino-Casallo, M. J. Gomez-Benito, S. Hervas-Raluy and J. M. Garcia-Aznar, Unravelling cell migration: defining movement from the cell surface, *Cell Adhes. Migr.*, 2022, **16**, 25–64.
55 E. Bahar and H. Yoon, Modeling and Predicting the Cell Migration Properties from Scratch Wound Healing Assay on Cisplatin-Resistant Ovarian Cancer Cell Lines Using Artificial Neural Network, *Healthcare*, 2021, **9**, 911.
56 K. M. Yamada, A. D. Doyle and J. Lu, Cell-3D matrix interactions: recent advances and opportunities, *Trends Cell Biol.*, 2022, **32**, 883–895.
57 V. Nica, A. Marino, C. Pucci, Ö. Şen, M. Emanet, D. De Pasquale, A. Carmignani, A. Petretto, M. Bartolucci,

S. Lauciello, R. Brescia, F. de Boni, M. Prato, S. Marras, F. Drago, M. Hammad, D. Segets and G. Ciofani, Cell-Membrane-Coated and Cell-Penetrating Peptide-Conjugated Trimagnetic Nanoparticles for Targeted Magnetic Hyperthermia of Prostate Cancer Cells, *ACS Appl. Mater. Interfaces*, 2023, **15**, 30008–30028.

58 N. Gupta, C. Gupta and H. B. Bohidar, Visible Laser Light Mediated Cancer Therapy via Photothermal Effect of Tannin-Stabilized Magnetic Iron Oxide Nanoparticles, *Nanomaterials*, 2023, **13**, 1456.

59 N. A. Franken, H. M. Rodermond, J. Stap, J. Haveman and C. Van Bree, Clonogenic assay of cells in vitro, *Nat. Protoc.*, 2006, **1**, 2315–2319.

60 A. Kinsner-Ovaskainen, J. Ponti, H. Norlén, S. Altmeyer, C. Andreoli, A. Bogni, S. Chevillard, I. De Angelis, S. Chung and I. Eom, Interlaboratory comparison study of the Colony Forming Efficiency assay for assessing cytotoxicity of nanomaterials, *Jt. Res. Cent.*, 2014, 1–80.

61 C. J. Malemud, Matrix metalloproteinases (MMPs) in health and disease: an overview, *Front. Biosci.-Landmark*, 2006, **11**, 1696–1701.

62 C. Wei, The multifaceted roles of matrix metalloproteinases in lung cancer, *Front. Oncol.*, 2023, **13**, 1195426.

63 N. Merchant, G. P. Nagaraju, B. Rajitha, S. Lammata, K. K. Jella, Z. S. Buchwald, S. S. Lakka and A. N. Ali, Matrix metalloproteinases: their functional role in lung cancer, *Carcinogenesis*, 2017, **38**, 766–780.

64 F. L. Tansi, F. Fröbel, W. O. Maduabuchi, F. Steiniger, M. Westermann, R. Quaas, U. K. Teichgräber and I. Hilger, Effect of Matrix-Modulating Enzymes on the Cellular Uptake of Magnetic Nanoparticles and on Magnetic Hyperthermia Treatment of Pancreatic Cancer Models In Vivo, *Nanomaterials*, 2021, **11**, 438.

65 J. S. Becker, A. Matusch and B. Wu, Bioimaging mass spectrometry of trace elements – recent advance and applications of LA-ICP-MS: A review, *Anal. Chim. Acta*, 2014, **835**, 1–18.

66 A. Babsky, S. K. Hekmatyar, T. Gorski, D. S. Nelson and N. Bansal, Heat-induced changes in intracellular Na+, pH and bioenergetic status in superfused RIF-1 tumour cells determined by 23Na and 31P magnetic resonance spectroscopy, *Int. J. Hyperthermia*, 2005, **21**, 141–158.

67 R. B. Mikkelsen and C. R. Asher, Effects of hyperthermia on the membrane potential and Na+ transport of V79 fibroblasts, *J. Cell. Physiol.*, 1990, **144**, 216–221.

68 J. L. Roti Roti, Cellular responses to hyperthermia (40–46 °C): Cell killing and molecular events, *Int. J. Hyperthermia*, 2008, **24**, 3–15.

69 R. P. Verma and C. Hansch, Matrix metalloproteinases (MMPs): chemical-biological functions and (Q)SARs, *Bioorg. Med. Chem.*, 2007, **15**, 2223–2268.

70 A. Varki, Biological roles of glycans, *Glycobiology*, 2016, **27**, 3–49.

71 K. Kawanishi, Y. Naito-Matsui, L. Soares Zaramela, N. M. van Sorge and M. Yamaguchi, Editorial: A sweet deal – Glycobiology in host-pathogen interactions, *Front. Microbiol.*, 2023, **14**, 1341820.

72 U. I. M. Gerling-Driessen, M. Hoffmann, S. Schmidt, N. L. Snyder and L. Hartmann, Glycopolymers against pathogen infection, *Chem. Soc. Rev.*, 2023, **52**, 2617–2642.

73 K. Hodgson, M. Orozco-Moreno, E. Scott, R. Garnham, K. Livermore, H. Thomas, Y. Zhou, J. He, A. Bermudez, F. J. Garcia Marques, K. Bastian, G. Hysenaj, E. Archer Goode, R. Heer, S. Pitteri, N. Wang, D. J. Elliott and J. Munkley, The role of GCNT1 mediated O-glycosylation in aggressive prostate cancer, *Sci. Rep.*, 2023, **13**, 17031.

74 R. Yun, E. Hong, J. Kim, B. Park, S. J. Kim, B. Lee, Y. S. Song, S.-J. Kim, S. Park and J. M. Kang, N-linked glycosylation is essential for anti-tumor activities of KIAA1324 in gastric cancer, *Cell Death Dis.*, 2023, **14**, 546.

75 Q. Zhu, H. Zhou, L. Wu, Z. Lai, D. Geng, W. Yang, J. Zhang, Z. Fan, W. Qin, Y. Wang, R. Zhou and W. Yi, O-GlcNAcylation promotes pancreatic tumor growth by regulating malate dehydrogenase 1, *Nat. Chem. Biol.*, 2022, **18**, 1087–1095.

76 Y. Meng, S. Sanlidag, S. A. Jensen, S. A. Burnap, W. B. Struwe, A. H. Larsen, X. Feng, S. Mittal, M. S. P. Sansom, C. Sahlgren and P. A. Handford, An N-glycan on the C2 domain of JAGGED1 is important for Notch activation, *Sci. Signaling*, 2022, **15**, eabo3507.

77 H. L. Chen, Lewis glyco-epitopes: structure, biosynthesis, and functions, *Adv. Exp. Med. Biol.*, 2011, **705**, 53–80.

78 S. S. Pinho and C. A. Reis, Glycosylation in cancer: mechanisms and clinical implications, *Nat. Rev. Cancer*, 2015, **15**, 540–555.

79 X. Xu, Q. Peng, X. Jiang, S. Tan, W. Yang, Y. Han, L. Oyang, J. Lin, M. Shen, J. Wang, H. Li, L. Xia, M. Peng, N. Wu, Y. Tang, H. Wang, Q. Liao and Y. Zhou, Altered glycosylation in cancer: molecular functions and therapeutic potential, *Cancer Commun.*, 2024, **44**, 1316–1336.

80 F. S. Coulibaly and B.-B. C. Youan, Concanavalin A–Polysaccharides binding affinity analysis using a quartz crystal microbalance, *Biosens. Bioelectron.*, 2014, **59**, 404–411.

81 H. Huldani, A. I. Rashid, K. N. Turaev, M. J. C. Opulencia, W. K. Abdelbasset, D. O. Bokov, Y. F. Mustafa, M. E. Al-Gazally, A. T. Hammid, M. M. Kadhim and S. H. Ahmadi, Concanavalin A as a promising lectin-based anti-cancer agent: the molecular mechanisms and therapeutic potential, *Cell Commun. Signaling*, 2022, **20**, 167.

82 W. I. Weis and K. Drickamer, Structural basis of lectin-carbohydrate recognition, *Annu. Rev. Biochem.*, 1996, **65**, 441–473.

83 B. Herrero de la Parte, I. Rodrigo, J. Gutiérrez-Basoa, S. Iturrizaga Correcher, C. Mar Medina, J. J. Echevarría-Uraga, J. A. Garcia, F. Plazaola and I. García-Alonso, Proposal of New Safety Limits for In Vivo Experiments of Magnetic Hyperthermia Antitumor Therapy, *Cancers*, 2022, **14**, 3084.

84 Q. A. Pankhurst, J. Connolly, S. K. Jones and J. Dobson, Applications of magnetic nanoparticles in biomedicine, *J. Phys. D: Appl. Phys.*, 2003, **36**, R167.

85 R. R. Shah, T. P. Davis, A. L. Glover, D. E. Nikles and C. S. Brazel, Impact of magnetic field parameters and iron

oxide nanoparticle properties on heat generation for use in magnetic hyperthermia, *J. Magn. Magn. Mater.*, 2015, **387**, 96–106.

86 O. L. Lanier, O. I. Korotych, A. G. Monsalve, D. Wable, S. Savliwala, N. W. F. Grooms, C. Nacea, O. R. Tuitt and J. Dobson, Evaluation of magnetic nanoparticles for magnetic fluid hyperthermia, *Int. J. Hyperthermia*, 2019, **36**, 686–700.

87 M. W. Dewhirst, B. L. Viglianti, M. Lora-Michiels, M. Hanson and P. J. Hoopes, Basic principles of thermal dosimetry and thermal thresholds for tissue damage from hyperthermia, *Int. J. Hyperthermia*, 2003, **19**, 267–294.

88 G. C. van Rhoon, T. Samaras, P. S. Yarmolenko, M. W. Dewhirst, E. Neufeld and N. Kuster, CEM43 °C thermal dose thresholds: a potential guide for magnetic resonance radiofrequency exposure levels?, *Eur. Radiol.*, 2013, **23**, 2215–2227.

89 B. L. Viglianti, M. W. Dewhirst, J. P. Abraham, J. M. Gorman and E. M. Sparrow, Rationalization of thermal injury quantification methods: Application to skin burns, *Burns*, 2014, **40**, 896–902.

90 Z. Vujaskovic, D. W. Kim, E. Jones, L. Lan, L. McCall, M. W. Dewhirst, O. Craciunescu, P. Stauffer, V. Liotcheva, A. Betof and K. Blackwell, A phase I/II study of neoadjuvant liposomal doxorubicin, paclitaxel, and hyperthermia in locally advanced breast cancer, *Int. J. Hyperthermia*, 2010, **26**, 514–521.

91 M. E. Reis, A. Bettencourt and H. M. Ribeiro, The regulatory challenges of innovative customized combination products, *Front. Med.*, 2022, **9**, 821094.

92 I. Baldea, C. Iacoviță, R. A. Gurgu, A. S. Vizitiu, V. Râzniceanu and D. R. Mitrea, Magnetic Hyperthermia with Iron Oxide Nanoparticles: From Toxicity Challenges to Cancer Applications, *Nanomaterials*, 2025, **15**, 1519.

93 M. Latorre and C. Rinaldi, Applications of magnetic nanoparticles in medicine: magnetic fluid hyperthermia, *P. R. Health Sci. J.*, 2009, **28**, 227–238.

94 J. Nowak-Jary and B. Machnicka, In vivo Biodistribution and Clearance of Magnetic Iron Oxide Nanoparticles for Medical Applications, *Int. J. Nanomed.*, 2023, **18**, 4067–4100.